Comput. Methods Appl. Mech. Engrg. 253 (2013) 219–236

Contents lists available at SciVerse ScienceDirect

Comput. Methods Appl. Mech. Engrg.

journal homepage: www.elsevier.com/locate/cma

On the spatial formulation of discontinuous Galerkin methods for finite elastoplasticity ☆

Ruijie Liu [a,*], Mary F. Wheeler [a], Ivan Yotov [b]

[a] Institute for Computational Engineering and Sciences, The University of Texas at Austin, Austin, TX 78712, USA
[b] Department of Mathematics, The University of Pittsburgh, Pittsburgh, PA 15260, USA

ARTICLE INFO

Article history:
Received 18 November 2011
Received in revised form 6 July 2012
Accepted 26 July 2012
Available online 4 August 2012

Keywords:
DG
Incomplete Interior Penalty Galerkin
Spatial formulation
Hypoelastoplasticity
Hyperelastoplasticity
Surface geometry stiffness

ABSTRACT

In this paper, we present a consistent spatial formulation for discontinuous Galerkin (DG) methods applied to solid mechanics problems with finite deformation. This spatial formulation provides a general, accurate, and efficient DG finite element computational framework for modeling nonlinear solid mechanics problems. To obtain a consistent formulation, we employ the Incomplete Interior Penalty Galerkin (IIPG) method. Another requirement for achieving a fast convergence rate for Newton's iterations is the consistent formulation of material integrators. We show that material integrators that are well developed and tested in continuous Galerkin (CG) methods can be fully exploited for DG methods by additionally performing stress returning on element interfaces. Finally, for problems with pressure or follower loading, stiffness contributed from loaded surfaces must also be consistently incorporated. In this work, we propose the Truesdell objective stress rate for both hypoelastoplastic and hyperelastoplastic problems. Two formulations based on the co-rotational and multiplicative decomposition-based frameworks are implemented for hypoelastoplasticity and hyperelastoplasticity, respectively. Two new terminologies, the so-called standard surface geometry stiffness and the penalty surface geometry stiffness, are introduced and derived through consistently linearizing the virtual work contributed from interior surface integrals. The performance of our DG formulation has been demonstrated through solving a cantilever beam problem undergoing large rotations, as well as a bipolar void coalescence problem where the voids grow up to several hundred times of their original volumes. Fast convergence rates for Newton's iterations have been achieved in our IIPG implementation.

1. Introduction

It is the objective of this paper to establish a consistent spatial formulation for discontinuous Galerkin (DG) methods applied to solid mechanics problems with finite deformation. Several good DG features such as locking-free for nearly incompressible materials suggest a great potential for DG methods to be used as an alternative to CG methods. On the other hand, in general, a full DG discretization for the entire domain may be expensive. For many practical applications, the coupled use of CG and DG methods has CPU advantages through locally employing DG elements. As shown in [19,45], DG methods provide a natural computational framework for modeling crack opening and shear band problems. Obviously, the use of DG elements only in areas near cracks or shear bands is much more efficient. In such situations, DG methods should be formulated in a framework that is consistent with CG methods. Furthermore, it is important to do this in both co-rotational and multiplicative decomposition-based frameworks for solving nonlinear solid mechanics problems with finite deformation. In this paper we develop a consistent spatial formulation for the IIPG method. Rather than demonstrating some specific advantages of DG over CG, numerical examples in this paper are selected to evaluate the performance of the IIPG method for solving large rotation and large deformation problems in terms of accuracy and convergence of the Newton's iteration.

The foundation for modeling finite deformation problems is the theory of nonlinear continuum mechanics [53,17,32,42]. The dominant finite element frameworks are CG-based. The pioneering CG nonlinear finite element analysis for nonlinear solid and structure continua has been developed by Oden in [40]. The work by Hughes and Pister [24] put forward the consistent linearization concept for substantially accelerating solutions for nonlinear problems in CG frameworks. For both hypoelastoplasticity and hyperelastoplasticity, the stress updating schemes and consistent algebraic modulus systematically obtained from the so-called local material integrators have been developed by [25,36,46,43,47,1,48,49,35] for classic

☆ This work was partially supported by DOE Grants DE-FG02-04ER25617 and DE-FG02-04ER25618.

* Corresponding author. Address: ANSYS INC., Southpointe, 275 Technology Drive, Canonsburg, PA 15317, USA.
E-mail addresses: Ruijie.Liu@ansys.com, rliu@ansys.com (R. Liu).

0045-7825/$ - see front matter © 2012 Published by Elsevier B.V.
http://dx.doi.org/10.1016/j.cma.2012.07.015

J_2 and pressure-sensitive plasticity models. The importance of these consistently formulated material integrators is in that complex practical elastoplasticity problems could be solved in tens or hundreds of loading steps rather than tens of thousands of loading steps required by the methods using continuous tangent elastoplastic modulus. This has motivated many commercial finite element codes to develop and implement consistently formulated material integrators.

Parallel to the development of CG methods, DG methods [38,14,4,55,2] have been proposed for reducing the errors induced by the strong implementation of Dirichlet boundary conditions in CG methods. A number of DG formulations for fluid problems have been presented in [9,41,7,10]. For elliptic problems, Arnold et al. [3] proposed a unified theoretical DG framework. For linear elasticity with small deformation, Hansbo and Larson [18], Riviere and Wheeler [44], Wihler [56], Lew et al. [26], and Liu et al. [28] demonstrated that DG methods are good alternatives to CG methods in avoiding volume locking issues. DG methods have been extended to nonlinear problems in the framework of small deformation by Wells et al. [54,34] for damage mechanics problems, by Liu et al. [27,29,30] for poromechanics problems, and by Hansbo [19], Liu et al. [31], and Djoko et al. [12,13] for classic plasticity problems with small deformation. For nonlinear solid mechanics with finite deformation, DG methods have been studied by Noels et al. [39] and Ten Eyck et al. [50,51] for hyperelasticity and by McBride et al. [33] for finite gradient plasticity problems.

We now address the contributions of this work. First, the total Lagrange formulation and the updated Lagrange (spatial) formulation are the two finite element frameworks for solving finite deformation problems. These two methods are theoretically equivalent. For practical applications, however, the spatial formulation is more popular in many commercial finite element codes. This is because the field variables obtained from the total Lagrange formulation are based on the reference configuration and have to be transformed into variables defined in the current configuration for visualization and data analysis purpose. On the other hand, the field variables, i.e., the Cauchy stress and the true stress, are naturally computed in the current configuration and can be directly visualized without any transformation. We therefore adopt a spatial DG formulation. This approach would also greatly facilitate the coupling between CG and DG methods. Detailed DG spatial formulations and implementations for solid mechanics problems with finite deformation are little documented in the literature. In this work, our DG formulation and linearization are performed on the current configuration through employing the spatial velocity and the material time derivative techniques.

Second, the co-rotational formulation [40] for hypoelastoplastic models and potential energy function-based formulation for hyperelastoplastic models are two major finite element frameworks for finite deformation problems. For practical applications, these two frameworks are equally important. The DG methods in [39,50,51,33] are formulated and tested on only hyperelasticity or hyperelastoplasticity. The robust implementation of the co-rotational formulation for finite hypoelasticity has been one of the most challenging topics for computer programming [21,22,52]. In this work, our DG methods are formulated and evaluated on both co-rotational and multiplicative decomposition-based frameworks, which are critical in many practical applications. Third, our DG spatial formulation for finite deformation problems is based on consistently linearizing nonlinear equations, which provides a fast convergence rate for Newton's iterations. In [39], the proposed DG method is symmetric and only for hyperelasticity. As discussed in [31], a family of DG methods, except for the Incomplete Interior Penalty Galerkin [11], have difficulties in achieving a consistent formulation for plasticity problems even with small deformation. A consistent DG formulation derived in [31] for classical plasticity problems is based on IIPG method, but only for problems with small deformation. In this work, we extend IIPG method to finite elastoplastic problems. Finally, the stiffness contributed from pressure loadings is also considered in our DG formulation, which is important for achieving fast convergence rates for Newton's iterations for modeling pressure vessel problems.

We organize the remaining sections of this paper as follows. In Section 2, we summarize the fundamentals of nonlinear continuum mechanics. The material time derivatives of a few deformation-related variables are summarized in this section for facilitating the linearization of our DG formulation. Mathematical statements for modeling finite deformation problems are defined in Section 3. We develop the spatial IIPG formulation in Section 4. The IIPG nonlinear equations are linearized in Section 5. Section 6 addresses the importance of establishing local material integrators for achieving consistent DG formulations. The spatial DG implementation and nonlinear solution procedures are discussed in Section 7. In Section 8, we present numerical examples to demonstrate the performance of our proposed IIPG method. Conclusions are summarized in Section 9.

2. Fundamentals of nonlinear continuum mechanics

In this section, referring to [32,49], we describe some key variables in nonlinear continuum mechanics. These include the deformation gradient, polar decomposition of the deformation gradient, and pairs of stress and strain measurements. More specifically, we summarize the rate change forms of the deformation gradient, infinitesimal volume, and infinitesimal surface area, which will greatly facilitate our linearization of the virtual work in DG frameworks performed in later sections. Objective stress rates are also summarized in this section.

2.1. Strain and stress measurements

Let $B_0 \subset R^3$ be the reference configuration and let $B_t \subset R^3$ be the current deformed configuration. As shown in Fig. 1, a one-to-one mapping $\phi(X,t)$ maps a particle $X \in B_0$ into $x \in B_t$:

$$x = \phi(X,t). \tag{1}$$

The material velocity V and spatial velocity v of the motion ϕ are defined as follows:

$$V(X,t) = \frac{\partial \phi(X,t)}{\partial t}, \quad v(x,t) = V(X,t) \circ \phi^{-1}(X,t), \tag{2}$$

where ϕ^{-1} is the inverse of the mapping function ϕ. The deformation gradient F is defined as the partial derivative of the mapping function ϕ with respective to the reference coordinates as follows:

$$F(X,t) = \frac{\partial \phi(X,t)}{\partial X}.$$

The deformation gradient F can be multiplicatively decomposed into a rotational tensor $R(X,t)$ and a stretch tensor $U(X,t)$ as follows:

$$F(X,t) = R(X,t)U(X,t), \tag{3}$$

where $U(X,t)$ is the right stretch tensor. The above equation is the polar decomposition of the deformation gradient and the rotational tensor $R(X,t)$ plays a key role in establishing co-rotational finite element frameworks for hypoelastoplasticity. The right Cauchy–Green tensor C and left Cauchy–Green tensor b are defined in terms of the deformation gradient F as follows:

$$C(X,t) = F^T F; \quad b(x,t) = FF^T,$$

where the superscript T indicates the transpose operation of tensors. Besides of the right Cauchy–Green and left Cauchy–Green

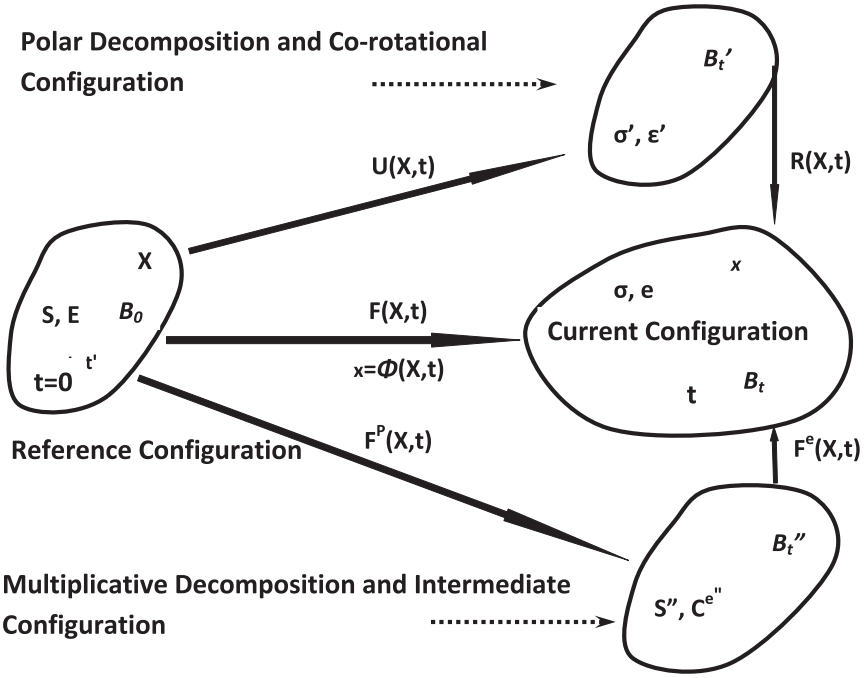

Fig. 1. Reference configuration, current configuration, co-rotational configuration, intermediate configuration, and stress–strain measurements of a continuum body.

tensors, two other important strain measurements are the Green–Lagrange (E) and the Almansi strain (e) tensors:

$$E(X,t)=\frac{1}{2}(C(X,t)-I);\quad e(x,t)=\frac{1}{2}(I-b^{-1}(x,t)),$$

where I is the second order identity tensor and the superscript -1 indicates the inverse operation of second order tensors. The Cauchy stress σ, the first Piola–Kirchhoff stress P, and the second Piola–Kirchhoff stress S are most frequently used for stress measurements. The first and the second Piola–Kirchhoff stresses can be pulled back using the Cauchy stress as follows:

$$P(X,t)=JF^{-1}\sigma(x,t);\quad S(X,t)=JF^{-1}\sigma(x,t)F^{-T},$$

where J is the determinant of the deformation gradient F. Three stress–strain conjugate pairs based on the energy power are grouped as follows:

$$(\sigma,e);\quad (P,F);\quad (S,E).$$

2.2. Rates of change in kinematics

The velocity gradient l is the partial derivative of the velocity with respective to the spatial coordinate x:

$$l(x,t)=\frac{\partial v(x,t)}{\partial x},$$

where $v(x,t)$ is the spatial velocity defined in (2). The rate of the deformation gradient tensor, d, and the spine tensor, w, can be written in terms of l as follows:

$$d=\frac{1}{2}(l+l^T);\quad w=\frac{1}{2}(l-l^T).$$

Without presenting the proof we simply summarize the material time derivatives of F, $J=det(F)$, F^{-1}, and infinitesimal volume dv, as well as the Nanson formula as follows:

$$\dot{F}=lF;\ \dot{J}=J\mathbf{trace}(l);\ \overrightarrow{\dot{F^{-1}}}=-F^{-1}l;\ \overrightarrow{d\dot{v}}=\mathbf{trace}(l)dv;\ \overrightarrow{ds}=JF^{-T}\overrightarrow{dS},\tag{4}$$

where the dot symbol over the heads of variables indicates the material time derivative operation and the combined use of the dot and bar symbols over the heads of variables is to avoid any confusions in the cases where variables are denoted by composite symbols. Note that $\overrightarrow{ds}=\vec{n}ds$ in (4) is a vector where $\vec{n}$ is the normal vector defined for an infinitesimal surface area ds. We refer to [23] (Pages 96–104) for the detailed proofs for the formulas in (4).

In the next two lemmas we introduce the so-called Lamb surface velocity gradient tensor and the rate of change of an infinitesimal surface area. The two lemmas will be employed to facilitate the linearization of our DG formulation involving face integrals in later sections.

As shown in Fig. 2, an infinitesimal surface area dS with its normal vector $\vec{N}$ in the reference configuration B_0 is dragged by the deformation gradient F into an infinitesimal surface area ds with its normal vector $\vec{n}$ in the current configuration B_t.

Lemma 1. *The rate of change of a vector element of an infinitesimal surface area in the current configuration B_t shown in Fig. 2 satisfies* $\overrightarrow{\dot{ds}}=(\mathbf{trace}(l)I-l^T)\overrightarrow{ds}$.

Proof. Using the Nanson formula given in (4) and performing the material time derivative operation on $\overrightarrow{ds}$, we obtain:

$$\begin{aligned}\overrightarrow{\dot{ds}}&=(\dot{J}F^{-T}+J\overrightarrow{\dot{F^{-T}}})\overrightarrow{dS}=(\mathbf{trace}(l)JF^{-T}-Jl^TF^{-T})\overrightarrow{dS}\\&=(\mathbf{trace}(l)I-l^T)JF^{-T}\overrightarrow{dS}=(\mathbf{trace}(l)I-l^T)\overrightarrow{ds},\end{aligned}$$

where the rates of change in (4) have been used. □

More precisely, Lemma 1 is the Lamb formula. The tensor $\mathbf{trace}(l)I-l^T$ is a strain rate measurement on surfaces in the current configuration. As shown in later DG linearization section, it plays a key role in dealing with the linearization of the virtual work contributed from surface integrals. Therefore, we call this tensor the Lamb surface velocity gradient tensor l_s defined as follows:

$$l_s=\mathbf{trace}(l)I-l^T.\tag{5}$$

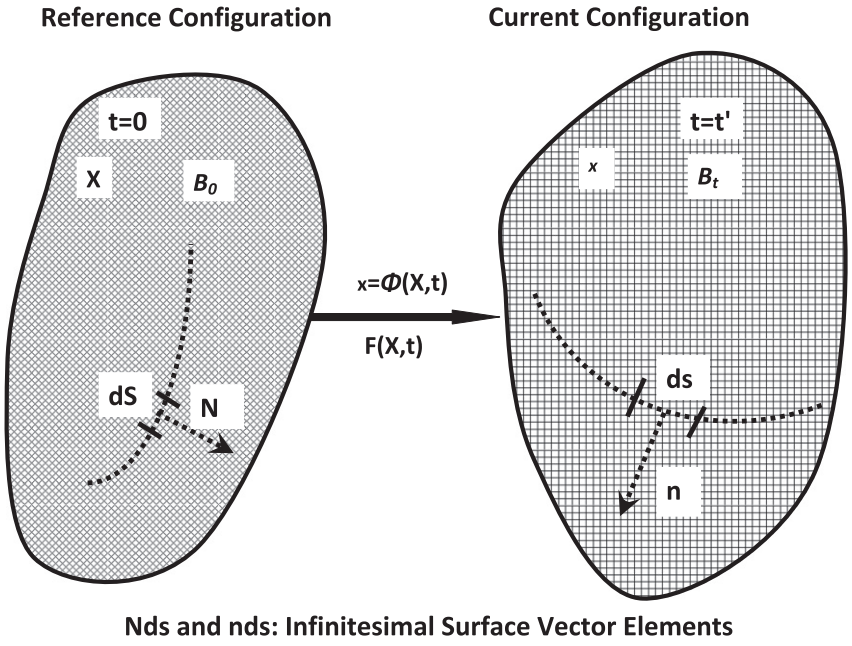

Fig. 2. Interior continuum surfaces in reference and current configurations.

Lemma 2. *The rate of change of an infinitesimal surface area* $ds \in R^+$ *in the current configuration* B_t *shown in Fig. 2 satisfies*

$$\dot{\overrightarrow{ds}} = (l_s \vec{n}) \cdot \vec{n} ds.$$

Proof. Decomposing $\overrightarrow{ds}$ into $\vec{n}$ and ds and applying Lemma1, we obtain:

$$\dot{\overrightarrow{ds}} = \dot{\vec{n}} ds + \vec{n} \dot{ds} = (\mathbf{trace}(l) I - l^T) \overrightarrow{ds} = l_s \overrightarrow{ds},$$

implying

$$\dot{\vec{n}} = l_s \vec{n} - \vec{n} \frac{\dot{ds}}{ds}. \tag{6}$$

Noting that the scalar variable ds can be rewritten as the scalar product of $\vec{n}$ and vector $\overrightarrow{ds}$, we obtain:

$$\dot{ds} = \dot{\vec{n}} \cdot \overrightarrow{ds} = \dot{\vec{n}} \cdot \overrightarrow{ds} + \vec{n} \cdot \dot{\overrightarrow{ds}} = \dot{\vec{n}} \cdot \vec{n} ds + \vec{n} \cdot (l_s \vec{n}) ds. \tag{7}$$

Inserting (6) into (7), we have:

$$2\dot{ds} = 2\vec{n} \cdot (l_s \vec{n}) ds. \qquad \square$$

In the next sections, we will omit $\rightarrow$ from vector $\vec{n}$ whenever no confusion occurs.

2.3. Objective stress rate

For materials with hypoelastoplastic models, constitutive laws are described in terms of stress rates. The stress rates must be objective so that the constitutive models are frame-indifferent. The material time derivative of the Cauchy stress $\dot{\sigma}$ resulting from the linearization of virtual work as shown in a later section is not objective and cannot be directly applied to enforce constitutive laws. The Truesdell, Jaumann–Zaremba, and Green–Naghdi stress rates are the most popular candidates for objective stress rates. The Truesdell stress rate σ^O can be written in terms of the Cauchy stress and the velocity gradient tensors as follows:

$$\sigma^O = \dot{\sigma} - l\sigma - \sigma l^T + \mathbf{trace}(l)\sigma, \tag{8}$$

or

$$\dot{\sigma} = \sigma^O + l\sigma + \sigma l^T - \mathbf{trace}(l)\sigma. \tag{9}$$

Rather than directly applying the Cauchy stress rate $\dot{\sigma}$, the Truesdell stress rate σ^O is selected for enforcing constitutive laws. All other terms in (9) will eventually contribute to form "geometrical stiffness" in finite element formulations. In this paper, we adopt the Truesdell stress rate for the co-rotational formulation for finite hypoelastoplasticity and the formulation based on the intermediate configuration for hyperelastoplasticity. For other objective stress rates, we refer to [49].

3. Finite elastoplasticity problem

Problems with finite deformation involve geometrical and material non-linearities. Hypoelastoplasticity and hyperelastoplasticity are two main and distinctive theories for finite deformation problems. Despite of several drawbacks and limitations, hypoelastoplastic models have been more popular in practical large-scale inelastic applications than hyperelastoplastic models. On the other hand, hyperelastoplastic models are derived from micro-mechanical behavior of single-crystal metal plasticity theories, whose importance and interest are increasing.

For finite deformation problems, the stress computation based on incorporating material laws must satisfy the requirement of material frame indifference. For hypoelasticity, a popular framework for satisfying this requirement is based on the co-rotational formulation [40,32]. The essence of this method is in that material laws are implemented in a rotated configuration, in which the principle of material frame indifference is preserved. In this framework, the strain rate tensor d is rotated to the co-rotational configuration B_t' shown in Fig. 1 through applying tensor R, the rotational tensor obtained from the polar decomposition on F defined in (3):

$$\dot{\varepsilon}' = R^T d, \tag{10}$$

where $\dot{\varepsilon}'$ is the strain rate in the rotated configuration. The rotated Cauchy stress σ' is then computed through following the same procedures as the cases for hypoelastoplasticity with small deformation. For example, σ' is computed as follows:

$$\sigma' = \mathbf{D}' : \{\varepsilon' - \varepsilon'^p\}, \tag{11}$$

where ε'^p is the plastic strain in the rotated configuration, and $\mathbf{D}'$ is the fourth order elasticity tensor. Once the rotated Cauchy stress σ' is updated in the rotated configuration, the Cauchy stress σ is obtained through rotating σ' back to the current configuration B_t as follows:

$$\sigma = R\sigma' R^T. \tag{12}$$

We now define a mathematical problem for finite hypoelastoplasticity as follows:

Find $u,\ \sigma,\ \varepsilon'^e,$ and ε'^p that satisfy

$$\begin{cases} \nabla \cdot \sigma + \mathbf{b} = 0; \\ R = FU^{-1}; \\ \dot{\varepsilon}' = R^T d; \\ \dot{\varepsilon}'^e = \dot{\varepsilon}' - \dot{\varepsilon}'^p; \\ \lambda' Y(\sigma', q') = 0; \\ \dot{\varepsilon}'^p = \lambda' \frac{\partial f(\sigma', q')}{\partial \sigma'}; \\ \dot{q}' = -\lambda' h(\sigma', q'); \\ \sigma' = \mathbf{D}' : \varepsilon'^e; \\ \sigma = R\sigma' R^T \end{cases} \tag{13}$$

with prescribed displacement and traction boundary conditions

$$\begin{cases} u = \overline{u} \quad \text{on } \Gamma_u; \\ \sigma n = \overline{t} \quad \text{on } \Gamma_t, \end{cases} \tag{14}$$

where $\overline{\Gamma}_u \cup \overline{\Gamma}_t = \partial B_t$, and complementary relations

$$\begin{cases} \lambda' = 0 \quad \text{if } Y < 0; \\ \lambda' > 0 \quad \text{if } Y = 0, \end{cases} \tag{15}$$

where u is the displacement, $\mathbf{b}$ the body force vector, ε'^e the rotated elastic stain, Y the material yield function, f the material plastic flow potential, h the material hardening function, λ' the proportional plastic scalar, and q' is the plasticity-related state variable. In (13), the operator ∇ indicates $\frac{\partial}{\partial x}$, the partial derivative with respective to the spatial coordinates.

On the other hand, the principle of material frame indifference is preserved in the most popular framework for finite hyperelastoplasticity problems through updating stress measurements in the so-called intermediate configuration B_t'' shown in Fig. 1. This intermediate configuration is obtained through multiplicatively decomposing the deformation gradient F as follows:

$$F = F^e F^p, \tag{16}$$

where F^e is the elastic contribution to F, and F^p the deformation due to plastic flow. Using (16), the spatial velocity gradient l can be additively decomposed into the elastic and plastic parts l^e and l^p as follows:

$$l = l^e + l^p = \dot{F}^e F^{e-1} + F^e \dot{F}^p F^{p-1} F^{e-1}. \tag{17}$$

The components l^e and l^p can be mapped back to the intermediate configuration B_t'' through applying the pull-back operation as follows:

$$l^{e\prime\prime} = F^{e-1}\dot{F}^e, \quad l^{p\prime\prime} = \dot{F}^p F^{p-1}, \tag{18}$$

where $l^{e\prime\prime}$ and $l^{p\prime\prime}$ are the elastic and plastic velocity gradients defined in the intermediate configuration B_t'', respectively. Again, the plastic velocity gradient $l^{p\prime\prime}$ (plastic strain rate), yield function, flow function, and hardening function are defined in B_t'' and in similar forms as those for plasticity with small deformation. The second Piola-Kirchhoff stress S'', a stress measurement in the intermediate configuration B_t'', is obtained as follows:

$$S'' = 2\frac{\partial W(F^e)}{\partial C^{e\prime\prime}}, \tag{19}$$

where $C^{e\prime\prime} = F^{e^T} F^e$ and W the hyperelastic potential. The corresponding inelastic strain measurements can be defined as $C^p = F^{p^T} F^p$ (defined in the reference configuration B_0). The Cauchy stress σ in B_t is obtained through applying the push-forward operation on S'' as follows:

$$\sigma = F^e S'' F^{e^T}/J^e$$

where J^e is the determinant of F^e.

Finally, a mathematical problem for finite hyperelastoplasticity may be defined as follows:

Find $u,\ \sigma,\ C^{e\prime\prime},$ and C^p that satisfy:

$$\begin{cases} \nabla \cdot \sigma + \mathbf{b} = 0; \\ F = F^e F^p; \\ l^{e\prime\prime} = F^{e-1}\dot{F}^e; \\ \lambda'' Y(S'', q'') = 0; \\ l^{p\prime\prime} = \lambda'' \frac{\partial f(S'', q'')}{\partial S''}; \\ \dot{q}'' = -\lambda'' h(S'', q''); \\ S'' = 2\frac{\partial W(F^e)}{\partial C^{e\prime\prime}}; \\ \sigma = F^e S'' F^{e^T}/J^e \end{cases} \tag{20}$$

with prescribed displacement and traction boundary conditions

$$\begin{cases} u = \overline{u} \quad \text{on } \Gamma_u; \\ \sigma n = \overline{t} \quad \text{on } \Gamma_t \end{cases} \tag{21}$$

and complementary relations

$$\begin{cases} \lambda'' = 0 \quad \text{if } Y < 0; \\ \lambda'' > 0 \quad \text{if } Y = 0, \end{cases} \tag{22}$$

where Y is the material yield function, f the material plastic flow potential, h the material hardening function, λ'' the proportional plastic scalar, and q'' the plasticity-related state variable.

4. DG formulation

In this section we focus on IIPG formulation for nonlinear elastoplasticity problems with finite deformation. We first briefly summarize some DG notation, and then present the IIPG formulation. The importance of the IIPG formulation and its potential alternatives for efficiently modeling nonlinear solid mechanics problems with some specific material models are also discussed in this section.

We follow the DG notations introduced in [44,31]. A physical domain $B_t \in R^3$ is discretized into a finite element set: $\boldsymbol{\chi} = \{e_1, e_2, \cdots, e_N\}$. We categorize surfaces into three subsets, the interior interfaces, the prescribed displacement boundary surfaces, and the prescribed traction boundary surfaces. The set of interior faces in the current configuration B_t is denoted by $S_i = \{s_1, s_2, \cdots, s_m\}$. Γ_u denotes the set of the prescribed displacement boundary surfaces and Γ_t is the set of the described traction boundary surfaces. The set of all surfaces is $S = S_i \cup \Gamma_u \cup \Gamma_t$. The DG approximation is based on piecewise polynomial functions that may be discontinuous across the elements. For an interface γ, let e_L and e_R denote the left and right neighboring elements and let n be a fixed normal vector on γ oriented from e_L to e_R. For a function w, let w_L and w_R denote its values on e_L and e_R, respectively. We now define the jump and average quantities as follows:

$$[w] = w^L - w^R; \quad \{w\} = \frac{1}{2}(w^L + w^R). \tag{23}$$

The finite element space of discontinuous piecewise polynomials for DG methods for general three dimensional problems is defined as follows:

$$D_r(\chi) = \{v : v|_e \in (P_r(e))^3 \quad \forall e \in \chi\}.$$

We are now ready to establish a DG framework for nonlinear solid mechanics problems. We multiply the governing equation $\nabla \cdot \sigma + \mathbf{b} = 0$ from the first equation in (13) by a test function δu, integrate by parts over each element, and sum over all elements to obtain:

$$\sum_{e\in\chi}\int_e \sigma(u) : \nabla(\delta u)\, dv - \sum_{e\in\chi}\int_{\partial e}(\sigma n_e)\cdot \delta u\, ds - \sum_{e\in\chi}\int_e \mathbf{b}\cdot\delta u\, dv = 0,$$

where n_e the outward unit normal to ∂e. Note that each interior face integral appears twice, from its left and right neighbors. Decomposing the interface set S into interior faces, prescribed traction boundary faces, and prescribed displacement boundary surfaces, and moving the traction and body force terms into the right hand side, we obtain:

$$\sum_{e\in\chi}\int_e \sigma(u) : \nabla(\delta u)\, dv - \sum_{\gamma\in S_i}\int_\gamma \{\sigma n\}\cdot[\delta u]\, ds = \sum_{\gamma\in\Gamma_t}\int_\gamma \bar{t}\cdot\delta u\, ds + \sum_{e\in\chi}\int_e \mathbf{b}\cdot\delta u\, dv. \tag{24}$$

It should be mentioned that the prescribed displacement boundary faces may be also enforced weakly for improving solutions near boundaries as formulated in [44,18,51]. In this work, we add interface stiffness into a CG program for finite deformation, in which the displacement boundary conditions are strongly enforced. We only apply DG to interior element faces, allowing for flexible coupling of DG and CG. As a result, the integrals representing the virtual work contributed from the prescribed displacement boundary surfaces are not present in (24). The above formulation is, in general, not stable. To stabilize it, we add a penalty surface integral in terms of the jump of the solution and the jump of the test function:

$$\sum_{e\in\chi}\int_e \sigma(u) : \nabla(\delta u)\, dv - \sum_{\gamma\in S_i}\int_\gamma \{\sigma n\}\cdot[\delta u]\, ds + \frac{\delta_p G_0}{h_0}\sum_{\gamma\in S_i}\int_\gamma [u]\cdot[\delta u]\, ds = \sum_{\gamma\in\Gamma_t}\int_\gamma \bar{t}\cdot\delta u\, ds + \sum_{e\in\chi}\int_e \mathbf{b}\cdot\delta u\, dv, \tag{25}$$

where δ_p, G_0, h_0 are the penalty parameter, the material initial shear strength, and the square root of the face area, respectively.

Remark 1. More precisely, the formulation in (25) follows the IIPG formulation proposed in [31]. Other DG formulations such as the SIPG and NIPG methods that have been successfully applied to linear elasticity with small deformation [18,44,26,28] could also be formulated for finite deformation problems through adding the term $\pm\sum_{\gamma\in S_i}\int_\gamma\{\sigma(\delta u)n\}\cdot[u]\, ds$. For example, a symmetric stiffness matrix may be obtained if SIPG is adopted. As addressed in [31], however, this extra term, causes a difficulty in evaluating the internal force contributed from this term, which will be eventually used to compute the residual force. This is because the internal force f^I has to be expressed as $f^I = \pm\sum_{\gamma\in S_i}\int_\gamma\{\bullet\}[u]\, ds$ where $[u]$ is the jump on solution. For plasticity problems, an explicit or simple format for $\{\bullet\}$ in terms of kinematic measurements is unavailable. On the other hand, $f^I = -\sum_{\gamma\in S_i}\int_\gamma[B^T]\{\sigma\}\, ds$ is always valid for the primary interface term $-\sum_{\gamma\in S_i}\int_\gamma\{\sigma n\}\cdot[\delta u]\, ds$ in (25) no matter what the material behavior is. This is because B is only related to the kinematic measurements (strain and normal direction n). Since the IIPG method doesn't have the term $\pm\sum_{\gamma\in S_i}\int_\gamma\{\sigma(\delta u)n\}\cdot[u]\, ds$, the difficulty is naturally avoided. In the cases of associative plasticity models, a consistent CG formulation always results in a symmetric tangent modulus, which has an advantage in CPU time. However, the IIPG method always results in a non-symmetric stiffness matrix even for associative plasticity models. This IIPG drawback may be circumvented using lifting-type DG formulations, which have been successfully applied to nonlinear elasticity problems with finite deformation by Ten Eyck and Lew [50]. The essence of these lifting DG methods is to transform jumps on faces into equivalent strain fields on element interiors, by which symmetric formulations may be preserved. We point out that future research effort is needed for consistently linearizing lifting operators in finite elastoplastic problems.

5. Linearization

Let δW be the difference of the left and right hand sides of (25) in the previous section, i.e., the virtual work in the DG method. Note that δW is nonlinear in terms of the displacement u and the virtual displacement δu. In general, the Newton–Raphson iteration method is applied for solving this nonlinear equation, which requires linearization of (25). More precisely, we must perform the directional derivative (Gateaux derivative) of δW along δu as follows: $D_{\delta u}\delta W(u) = \frac{d}{d\eta}\delta W(u+\eta\delta u)|_{\eta\to 0}$ for obtaining the tangent modulus. A standard Gateaux's derivative procedure for linearizing the virtual work derived for spatial CG framework is well documented in the work of Holzapfel [23]. In this procedure, the linearization on the virtual work derived in the spatial formulation is actually performed in the reference configuration B_0 through transferring all spatial measurements into measurements defined in the reference configuration. The linearized measurements in B_0 are then transferred back to the current configuration B_t.

However, the Gateaux's derivative procedure involves extensive and complex pull-back and push-forward operations for finite deformation problems. To avoid these complex pull-back and push-forward operations, a technique based on material time derivatives of stress and strain measurements for linearizing the virtual work defined in the spatial formulation was developed by Holzapfel [23]. In this technique, performing the material derivative for the virtual work derived in the current configuration is equivalent to performing Gateaux's derivative in the reference configuration and is able to save the work of pull-back and push-forward operations. The material time derivative is performed in the spatial configuration and a complete linearization for the virtual work derived in the spatial formulation is obtained through simply replacing the velocity by the incremental displacement. A detailed procedure based on the material time derivative for linearizing the nonlinear equations resulting from CG spatial formulations for finite deformation problems is also summarized in [23] (see pages 399–401). It would be even more cumbersome to perform standard Gateaux derivative for DG formulations because several extra face integrals also have to be linearized. In this paper, to keep a concise derivation, we adopt the material time derivative technique developed in [23] to linearize Eq. (25).

The material time derivatives of volume, surface area, stress, and strain variables introduced in Section 2 are available to use in the linearization via the material time derivative technique. However, we still need two more material time derivatives, $\dot{\delta u}$ and $\dot{\nabla}(\delta u)$.

The material time derivatives of test functions or virtual displacements δu satisfy $\dot{\delta u} = 0$. However, $\dot{\nabla}(\delta u) = (\frac{\partial \dot{\delta u}}{\partial x})$ does not vanish since the spatial coordinate x depends on solution u, but it can be shown that

$$\dot{\overline{\nabla\delta u}} = -\nabla\delta u\, l. \tag{26}$$

To prove (26), we note that

$$\nabla\delta u = \frac{\partial\delta u}{\partial x} = \frac{\partial\delta u}{\partial X}\frac{\partial X}{\partial x} = \frac{\partial\delta u}{\partial X}\left\{\frac{\partial x}{\partial X}\right\}^{-1} = \frac{\partial\delta u}{\partial X}F^{-1} \tag{27}$$

and

$$\dot{\overline{\nabla\delta u}} = \dot{\overline{\frac{\partial\delta u}{\partial X}F^{-1}}} = -\frac{\partial\delta u}{\partial X}F^{-1}l = -\frac{\partial\delta u}{\partial x}l = -\nabla\delta u l, \tag{28}$$

where $\dot{\overline{F^{-1}}} = -F^{-1}l$ in (4) has been utilized.

We are now ready to linearize (25). Denoting the first term in (25) by δW_1, its material time derivative is

$$\dot{\overline{\delta W_1}} = \sum_{e\in\chi}\int_e \left(\dot{\overline{\sigma(u)}} : \nabla\delta u\, dv + \sigma(u) : \dot{\overline{\nabla\delta u}}\, dv + \sigma(u) : \nabla\delta u\, \dot{\overline{dv}}\right). \tag{29}$$

Inserting (9) for $\dot{\sigma}$, (28) for $\dot{\overline{\nabla\delta u}}$, and (4) for $\dot{\overline{dv}}$ into (29) and simplifying the result, we obtain the linearized $\dot{\overline{\delta W_1}}$:

$$\dot{\overline{\delta W_1}} = \sum_{e\in\chi}\int_e \left(\sigma^O : \nabla\delta u + l\sigma(u) : \nabla\delta u\right) dv. \tag{30}$$

Material constitutive laws will be enforced through the first term on the right hand side of (30). The second term on the right hand side of (30) represents the volume geometric stiffness. We note that (30) is just the spatial formulation for traditional displacement-based CG methods for finite deformation problems, which deals with only element volume integrals.

For the second term in (25), denoted by δW_2, we perform the material time derivative operation for this surface integral as follows, using $\dot{\overrightarrow{ds}} = nds$:

$$\begin{aligned}\dot{\overline{\delta W_2}} &= \dot{\overline{-\sum_{\gamma\in S_i}\int_\gamma \{\sigma n\}\cdot[\delta u]\, ds}} = \dot{\overline{-\sum_{\gamma\in S_i}\int_\gamma \{\sigma\overrightarrow{ds}\}\cdot[\delta u]}} \\ &= -\sum_{\gamma\in S_i}\int_\gamma \{\dot{\sigma}\overrightarrow{ds} + \sigma\dot{\overrightarrow{ds}}\}\cdot[\delta u].\end{aligned} \tag{31}$$

Inserting (9) for $\dot{\sigma}$ and applying Lemma1 for $\dot{\overrightarrow{ds}}$, we obtain

$$\begin{aligned}\dot{\overline{\delta W_2}} = -\sum_{\gamma\in S_i}\int_\gamma &\left\{\sigma^O + l\sigma + \sigma l^T - \mathbf{trace}(l)\sigma + \sigma(\mathbf{trace}(l)I - l^T)\right\} \\ &\overrightarrow{ds}\cdot[\delta u].\end{aligned} \tag{32}$$

Simplifying and applying $\dot{\overrightarrow{ds}} = nds$ to (32) again, we obtain:

$$\dot{\overline{\delta W_2}} = -\sum_{\gamma\in S_i}\int_\gamma \{\sigma^O + l\sigma\}n\cdot[\delta u]\, ds. \tag{33}$$

In (33), the material contribution to surface stiffness is obtained through utilizing the objective stress rate σ^O. The term $l\sigma$ in (33) represents a new geometric stiffness contribution from surface integrals. We call it the surface geometric stiffness.

We now linearize the third term in (25). Denoting this term by δW_3 and noting that δ_p, G_0, and h_0 are assumed to be constant, we have:

$$\dot{\overline{\delta W_3}} = \sum_{\gamma\in S_i}\frac{\delta_p G_0}{h_0}\int_\gamma \left([\dot{u}]\cdot[\delta u]\, ds + [u]\cdot[\delta u]\dot{\overline{ds}}\right). \tag{34}$$

Inserting the formula in Lemma 2 for $\dot{\overline{ds}}$ into (34), we complete the linearization of δW_3:

$$\dot{\overline{\delta W_3}} = \sum_{\gamma\in S_i}\frac{\delta_p G_0}{h_0}\int_\gamma \left([\dot{u}]\cdot[\delta u] + \{(l_s n)\cdot n\}[u]\cdot[\delta u]\right) ds. \tag{35}$$

It is evident from (35) that the stabilization term in the IIPG method also contributes to the geometric stiffness, which is related to the Lamb surface velocity gradient tensor l_s. We call this contribution the surface penalty geometric stiffness.

Similar to CG formulations, for the case $\mathbf{b} = \rho g$ with constant gravity, there is no stiffness contribution from the second term on the right hand side in (25). This can be verified as follows:

$$\begin{aligned}\dot{\overline{\delta W_4}} &= \dot{\overline{\sum_{e\in\chi}\int_e \rho g\cdot\delta u\, dv}} = \dot{\overline{\sum_{e\in\chi}\int_e \frac{\rho_0}{J}g\cdot\delta u\, dv}} \\ &= \sum_{e\in\chi}\int_e \rho_0 g\left(\dot{\overline{\left(\frac{1}{J}\right)}}dv + \frac{1}{J}\dot{\overline{dv}}\right)\cdot\delta u = 0\end{aligned} \tag{36}$$

where the material time derivatives of J and dv in (4) are utilized.

Finally, we work on the traction-related term, which is the first term on the right hand side in (25). In finite element frameworks, there would be no contribution to the stiffness from this term if the traction is converted to constant nodal forces at the stage of loading input. However, if the traction is a function of the deformation of the body or belongs to "follower" loading, the stiffness contributed from this traction term must be taken into account. Here we consider more general cases where the traction may be described as a function of deformation. In this case it is necessary to linearize the traction-related term in (25). Consequently, the stiffness contribution from loaded surfaces is obtained through applying the material time derivative to the first right hand side term in (25) as follows:

$$\dot{\overline{\delta W_5}} = \sum_{\gamma\in\Gamma^t}\int_\gamma \left(\dot{\bar{t}}\cdot\delta u + ((l_s n)\cdot n)\bar{t}\cdot\delta u\right) ds. \tag{37}$$

In the case of structures under pressure loading, the traction is defined in terms of the normal direction of pressured surfaces:

$$\bar{t} = -pn, \tag{38}$$

where n is the outward normal vector of loaded surfaces and p a scalar. A positive p value indicates a compressive loading behavior. For pressure loading, we obtain:

$$\begin{aligned}\dot{\overline{\delta W_6}} &= \dot{\overline{-\sum_{\gamma\in\Gamma^p}\int_\gamma pn\cdot\delta u ds}} = -\sum_{\gamma\in\Gamma^p}\int_\gamma p\dot{\overrightarrow{ds}}\cdot\delta u \\ &= -\sum_{\gamma\in\Gamma^p}\int_\gamma pl_s\overrightarrow{ds}\cdot\delta u = -\sum_{\gamma\in\Gamma^p}\int_\gamma pl_s n\cdot\delta u ds,\end{aligned} \tag{39}$$

where $\Gamma^p \subseteq \Gamma^t$ is defined for pressure boundary surfaces, scalar p itself is independent of the deformation of the body, and Lemma 1 is used.

To complete the linearization on IIPG formulation, we now collect the linearized δW_1 through δW_6 to obtain:

$$\begin{aligned}\dot{W} = \sum_{i=1}^{6}\dot{\overline{\delta W_i}} &= \sum_{e\in\chi}\int_e (l : \mathbf{c} : \nabla\delta u + l\sigma : \nabla\delta u)\, dv \\ &- \sum_{\gamma\in S_i}\int_\gamma \{\mathbf{c} : l + l\sigma\}n\cdot[\delta u]\, ds + \sum_{\gamma\in S_i}\frac{\delta_p G_0}{h_0}\int_\gamma ([\dot{u}]\cdot[\delta u] \\ &+ \{l_s : n\otimes n\}[u]\cdot[\delta u])\, ds - \sum_{\gamma\in\Gamma^t/\Gamma^p}\int_\gamma \left(\dot{\bar{t}}\cdot\delta u + (l_s : n\otimes n)\bar{t}\cdot\delta u\right) ds \\ &+ \sum_{\gamma\in\Gamma^p}\int_\gamma pl_s n\cdot\delta u ds,\end{aligned} \tag{40}$$

where material constitutive laws are incorporated into the formulation through $\sigma^O = \mathbf{c} : d$ as this stress rate is now objective, and the property $d : \mathbf{c} : \nabla\delta u = l : \mathbf{c} : \nabla\delta u$ and the minor symmetry of $\mathbf{c}$ have been used (see [23] page 400 for a CG-based spatial formulation).

As the linearized results in (40) are written in terms of the spatial velocity gradient l, we next discuss the discretization and integration in the time domain. We simply follow the scheme introduced in [23] (page 401) and replace the spatial velocity v by the incremental displacement:

$$\Delta u = \int_{t^n}^{t^{n+1}} v\, dt \approx v(x^{n+1})\Delta t = v(x^n + \Delta u)\Delta t,$$

where Δu is the incremental displacement from time t^n to time t^{n+1} and x^n the previous known spatial coordinate at time t^n. More precisely, this is the Euler backward integration scheme as x^{n+1}, the current coordinate of a point, is continuously updated through $x^{n+1} = x^n + \Delta u$ during each Newton's iteration for a given load step. Correspondingly, for the time discretization the material time derivative of displacement $\dot{u}$, the velocity gradient l, the Lamb surface velocity gradient l_s, and $\dot{\bar{t}}$ are replaced by:

$$\Delta u, \quad \mathbf{grad}(\Delta u), \quad g^{\Delta u} = \mathbf{trace}(\mathbf{grad}(\Delta u))I - \mathbf{grad}^T(\Delta u), \quad \text{and} \quad \Psi(\Delta u), \tag{41}$$

where $\mathbf{grad} \equiv \nabla$ and we need to address $\Psi(\Delta u)$ for replacing $\dot{\bar{t}}$ in (41). Depending on material properties on surfaces, $\dot{\bar{t}}$ could be formulated in terms of either $\mathbf{grad}(\Delta u)$ or Δu itself. Here, Ψ, a vector function of Δu, is understood. Substituting (41) into (40), we obtain the following incremental form of linearized virtual work:

$$\begin{aligned}
\Delta W = \sum_{i=1}^{6} \overline{\Delta W_i} = {} & \sum_{e\in\chi} \int_e (\mathbf{grad}\Delta u : \mathbf{c} : \mathbf{grad}\delta u + \mathbf{grad}\Delta u\, \sigma : \mathbf{grad}\delta u)\, dv \\
& - \sum_{\gamma\in S_i} \int_\gamma \{\mathbf{c} : \mathbf{grad}\Delta u + \mathbf{grad}\Delta u\, \sigma\} n \cdot [\delta u]\, ds \\
& + \sum_{\gamma\in S_i} \frac{\delta_p G_0}{h_0} \int_\gamma \left([\Delta u]\cdot[\delta u] + \left(g^{\Delta u} : n\otimes n\right)[u]\cdot[\delta u]\right) ds \\
& - \sum_{\gamma\in \Gamma^t/\Gamma^p} \int_\gamma \left(\Psi(\Delta u)\cdot\delta u + \left(g^{\Delta u} : n\otimes n\right)\bar{t}\cdot\delta u\right) ds \\
& + \sum_{\gamma\in\Gamma^p} \int_\gamma p\, g^{\Delta u} n\cdot\delta u\, ds.
\end{aligned} \tag{42}$$

Remark 2. In CG spatial formulations, the geometric stiffness is obtained through performing only volume integrations. As expected, besides the geometric stiffness from volume integration, interior surfaces introduced in DG methods also contribute to the geometric stiffness. More precisely, two additional geometric stiffnesses, one from the standard face integral and the other from the stabilization face integral, as shown in (40), are required for consistent spatial DG formulations. Although the geometric stiffness contribution from the stabilization face integrals may be negligible for some cases where the magnitude of the primary solution u is several orders lower than the Cauchy stress present in other geometric stiffnesses, it should be always included in DG implementations to avoid slow convergence rates in solving more general problems.

Remark 3. Through the linearization of the IIPG formulation, we underline that the so-called Lamb surface velocity gradient tensor, l_s, is very useful in dealing with surface-related rate of change. This is evident in that the rate of change of infinitesimal surface area simply satisfies $\dot{\overline{ds}} = n\cdot l_s n\, ds$ or $\dot{\overline{ds}} = (n\otimes n) : l_s\, ds$, which has been shown in Lemma2. Consequently, the geometric stiffness resulting from linearizing the stabilization interior face integrals and distributed loading boundary face integrals has a simple representation in terms of l_s. It should be noted that the derivation for the geometric stiffness contributed from "follower" or pressure loading was originally proposed in [20]. However, the derivation in [20] may be relatively complicated for implementation as the natural coordinates are involved and vector cross products are present. Since the natural coordinates do not appear in (40), the implementation of all geometric stiffness contributions simply follows well established volume and surface integrations in DG frameworks.

Remark 4. For linear elasticity problems with small deformation, the coercivity of the DG methods proposed in [44,18] is proved through exploiting the elliptic property of the fourth order elasticity tensor and applying sufficiently large penalty. The OBB DG method originally proposed in [41] for fluid problems and later applied to nearly incompressible elasticity [28] is naturally coercive. As shown in [31], for elastoplastic problems with small deformation the coercivity of the IIPG formulation is also satisfied if associative plasticity models with hardening are assumed. The coercivity analysis in [31] is solely based on good material properties, and the geometric stiffness is not taken into account. However, in addition to the major stiffness contributed from materials, geometric stiffness in terms of stresses also appears in linearized formulations of CG methods for finite deformation problems through volume integration. In our linearized spatial DG formulation for finite deformation problems, besides the volume geometric contribution, three additional geometric contributions including the standard, penalty, and traction boundary face integrals are also present. These geometric contributions should also be taken into account in any coercivity analysis for DG methods for finite deformation problems. In the case of the deformation of structures undergoing a compressive buckling dominated mode, the stiffness is singular, which indicates that the coercivity is lost in the buckling case. This suggests that the coercivity may not hold for linearized CG or DG formulations for general finite deformation problems. As discussed by Ten Eyck and Lew [51], however, the stability of linearized finite element formulations can be greatly improved by DG methods through applying appropriate penalty or stabilization parameters.

6. Material integrator

To achieve fast convergence rates for Newton's iterations for solving finite elastoplastic problems, consistent formulations on both geometric and material stiffnesses are required. The geometric stiffness contributions have been derived in the previous section. It is the focus of this section to address the stiffness contribution from materials. We first outline the procedures to implement hypoelastoplastic models in the co-rotational framework. In this framework, the strain rate tensor d in B_t is rotated to the rotated domain and then additively decomposed into the rate of elastic strain and plastic strain. The stress is updated in this rotated configuration (co-rotational domain). For hyperelastoplastic models, the stress updating is performed in the intermediate configuration. In this section we establish material integrators for updating stress and providing consistent tangent modulus for the Gaussian integration points on both elements and surfaces.

In (40), material laws are incorporated through the Truesdell stress rate. This approach unifies the formulations for both co-rotational and multiplicative decom-position-based frameworks. For the co-rotational implementation for hypoelastoplasticity, we follow a modified version of the Lie derivative discussed in [6] (p.260–262):

$$\sigma^{\circ} = R\dot{\sigma}' R^T,$$

and σ' can be updated in the rotated configuration B_t'. In time step $n+1$, the deformation gradient F^{n+1} is computed as:

$$F^{n+1} = I + \mathbf{Grad}(u^{n+1}),$$

where the symbol **Grad** indicates the partial derivative with respect to the reference coordinate X. The deformation gradient F^{n+1} is decomposed into the stretch tensor U^{n+1} and the rotational tensor R^{n+1} through the polar decomposition as follows:

$$F^{n+1} = R^{n+1}U^{n+1}. \tag{43}$$

The incremental strain is computed using the rate of deformation tensor d and the backward Euler integration method:

$$\Delta\varepsilon = \Delta t\, d = \frac{1}{2}(\mathbf{grad}(\Delta u) + \mathbf{grad}^{\mathbf{T}}(\Delta u)).$$

Using the rotational tensor R^{n+1} obtained from (43), the incremental strain $\Delta\varepsilon$ defined in the current configuration B_t can be transferred into an incremental strain $\Delta\varepsilon'$ in the co-rotational domain through the pull-back operation:

$$\Delta\varepsilon' = {R^{n+1}}^T \Delta\varepsilon R^{n+1}. \tag{44}$$

Having $\Delta\varepsilon'$ available, we now define the local material integrator problem for hypoelastoplastic materials in the rotated domain B'_t as follows:

Material integrator I: *Given* $(\sigma'^n, \varepsilon^{e'^n}, \varepsilon^{p'^n}, q'^n)$ *at time step n and the incremental strain* $\Delta\varepsilon'$ *for current time step* $n+1$ *in the rotated domain* B'_t, *find* $(\sigma'^{n+1}, \varepsilon^{e'^{n+1}}, \varepsilon^{p'^{n+1}}, q'^{n+1}, \mathbf{c}'^{n+1} = \frac{\partial\sigma'^{n+1}}{\partial\varepsilon'^{n+1}})$ *in the rotated domain* B'_t *at the current time step* $n+1$.

In this problem statement, $\varepsilon^{e'}$, $\varepsilon^{p'}$, q', and $\mathbf{c}'$ are, respectively, the elastic strain, plastic strain, plasticity-related state variable, and tangent modulus defined in the rotated or co-rotational domain B'_t. It is necessary to derive material integrators in a systematic way, in which both the stress returning and the consistent elastoplasticity tensor are constructed simultaneously. For finite deformation, many material integrators well developed for small deformation can be fully exploited through simply performing stress returning in the rotated configuration. For these material integrators, we refer to [47]. In this work, J_2 and rate-dependent plasticity with hardening models are implemented by following procedures reported in [31], where a material integrator for J_2 plasticity is proposed for the IIPG method for solving small deformation problems in the framework of hypoelastoplasticity.

Finally, the updated stress σ'^{n+1} together with the tangent modulus $\mathbf{c}'^{n+1}$ are transferred to the current configuration B_t through the push forward operation:

$$\sigma^{n+1} = R^{n+1}\sigma'^{n+1}{R^T}^{n+1}, \quad \mathbf{c}^{n+1}_{ijkl} = R_{im}R_{jn}R_{kp}R_{lq}\mathbf{c}^{primen+1}_{mnpq}. \tag{45}$$

The updated Cauchy stress σ^{n+1} and the consistent tangent modulus $\mathbf{c}^{n+1}$ are now spatially defined in the current configuration B_t and can be applied to form the stiffness and the residual force by following the spatial formulation in (48) and (49) for the next global nonlinear iteration.

We now focus on the hyperelastoplastic case. As discussed in Section 3, the total stress can be directly computed through taking the partial derivative of potential functions with respective to strain measurements. For the multiplicative framework, the strain energy W may be defined in terms of the elastic right Cauchy–Green strain tensor $C^{e''}$ defined in the intermediate configuration B''_t shown in Fig. 1 and the elasticity tensor in this intermediate configuration is obtained as follows:

$$\mathbf{c}^{\mathbf{e}''} = 4\frac{\partial^2 W(C^{e''})}{\partial C^{e''2}}. \tag{46}$$

Material yield, flow, and hardening functions are all defined in B''_t as previously discussed in Section 3. A typical construction of local material integrators based on the intermediate configuration can be found in [35]. The updated stress and tangent modulus obtained from such integrators have to be further pushed forward into the current configuration B_t for the spatial finite element formulation.

However, for the case where the elastic potential, yield, flow, and hardening functions are defined in terms of strain measurements in the current configuration B_t, the Cauchy stress and the tangent modulus can be directly constructed in the current configuration B_t as shown in [49]. Moreover, in the cases of isotropic hyperelastoplastic materials with elastic potentials in terms of stretches, a complete and efficient spatial-based material integrator can be found in Bonet and Wood [8]. In this paper, we simply follow the constructing procedures documented in [8] for neo-Hookean's materials with J_2 plasticity. The strain potential is defined as a function of the logarithmic stretches:

$$W(\lambda^e_1, \lambda^e_2, \lambda^e_3) = \frac{\lambda}{2}(\ln J^e) + \mu[(\ln\lambda^e_1)^2 + (\ln\lambda^e_2)^2 + (\ln\lambda^e_3)^2],$$

where $J^e = \lambda^e_1\lambda^e_2\lambda^e_3$ and λ and μ are the Lame constant and shear modulus. The quantities λ^e_i $(i = 1,2,3)$ are the principle stretches of the elastic finger tensor b^e defined in the current configuration B_t as follows:

$$b^e = FC^{p-1}F^T.$$

The yield and flow functions are written in terms of the Cauchy stress as follows:

$$Y(\sigma, \sigma_0(\bar{\varepsilon}^p)) = f(\sigma, \sigma_0(\bar{\varepsilon}^p)) = \sqrt{\frac{3}{2}\mathrm{dev}(\sigma) : \mathrm{dev}(\sigma)} - \sigma_0(\bar{\varepsilon}^p),$$

where $\mathrm{dev}(\sigma)$ is the deviatoric stress tensor, σ_0 the yield stress, and $\bar{\varepsilon}^p$ the equivalent plastic strain. A bilinear hardening model is implemented in this paper. We are now ready to define the local material integrator problem for hyperelastoplastic materials as follows:

Material integrator II: *Given* $(C^{p^n}, \bar{\varepsilon}^{p^n})$ *at time step n and the deformation gradient* F^{n+1} *at the current time step* $n+1$, *find* $(\sigma^{n+1}, C^{p^{n+1}}, \mathbf{c}^{n+1})$ *at the current time step* $n+1$.

In the above, $\mathbf{c}^{n+1}$ is the spatial consistent tangent modulus. For a detailed procedure for constructing Material Integrator II, we refer to [8] (p.212–214).

7. DG implementation and nonlinear procedure

The objective of this section is to describe the DG implementation based on the linearized results in the previous sections, as well as the global nonlinear Newton iteration. We present the DG tangent stiffness matrix and residual force vector. The consistent implementation for solving nonlinear problems via the Newton method requires not only to form the tangent stiffness matrix through consistently linearizing nonlinear equations, but also to correctly compute the residual force vector without dropping any of the terms in the DG formulation. Letting $\mathbf{\Delta U}$ be the nodal displacement incremental vector, then the incremental displacement Δu, the spatial gradient $\mathbf{grad}\Delta u$, its transpose $\mathbf{grad}^T\Delta u$, its trace $\mathbf{trace}(\mathbf{grad}\Delta u)$ and the Lamb surface gradient $g^{\Delta u}$ for an element interior point or a point on a surface can be interpolated in terms of $\mathbf{\Delta U}$:

$$\begin{cases} \Delta u = \mathbf{N}\,\mathbf{\Delta U}; \\ \mathbf{grad}\Delta u = \mathbf{L}\,\mathbf{\Delta U}; \\ \mathbf{grad}^T\Delta u = \mathbf{L_T}\,\mathbf{\Delta U}; \\ \mathbf{trace}(\mathbf{grad}\Delta u)I = \mathbf{L_0}\,\mathbf{\Delta U}; \\ g^{\Delta u} = (\mathbf{L_0} - \mathbf{L_T})\,\mathbf{\Delta U}; \\ \Psi^{\Delta u} = \Psi^{\bar{t}}\,\mathbf{\Delta U}, \end{cases} \tag{47}$$

where $\mathbf{N}, \mathbf{L}, \mathbf{L_T}, \mathbf{L_0}$, and $\Psi^{\bar{t}}$ are interpolation matrices. It should be noted that $\mathbf{L_T}$ is not the same as $\mathbf{L}$ or its transpose $\mathbf{L}^T$ due to the non-symmetry of the spatial displacement gradient tensor $\mathbf{grad}\Delta u$.

Inserting the interpolated variables from (47) into (42), we obtain the tangent stiffness matrix $\mathbf{K}$:

$$\begin{aligned}\mathbf{K} = &\sum_{e\in\chi}\int_e \mathbf{L}^{\mathbf{T}}(\mathbf{C}+\Lambda^{\sigma})\mathbf{L}\,dv - \sum_{\gamma\in S_i}\int_\gamma [\mathbf{N}^{\mathbf{T}}]\mathbf{n}\{(\mathbf{C}+\Lambda^{\sigma})\mathbf{L}\}\,ds\\ &+\sum_{\gamma\in S_i}\frac{\delta_p G_0}{h_0}\int_\gamma ([N^T][N]+[N^T]\Lambda^{[u]}\mathbf{n}^T\mathbf{n}\{L_0-L_T\})\,ds\\ &-\sum_{\gamma\in\Gamma^t/\Gamma^p}\int_\gamma \mathbf{N}^{\mathbf{T}}(\Psi^{\bar{\mathbf{t}}}+\Lambda^{\bar{\mathbf{t}}}\mathbf{n}^T\mathbf{n}(\mathbf{L_0}-\mathbf{L_T}))\,ds\\ &+\sum_{\gamma\in\Gamma^p}\int_\gamma p\mathbf{N}^{\mathbf{T}}\mathbf{n}(\mathbf{L_0}-\mathbf{L_T})\,ds, \end{aligned} \tag{48}$$

where Λ^{σ}, $\Lambda^{[\mathbf{u}]}$, $\Lambda^{\bar{\mathbf{t}}}$, and $\mathbf{n}$ are geometric matrices written in terms of stress, jump displacement, prescribed traction, and face normal directional components, respectively. In (48), $\mathbf{C}$ is the matrix form of the fourth-order consistent tangent modulus and a constant pressure loading case is assumed. The residual force vector $\mathbf{R}^{\mathbf{F}}$ that appears on the right hand side of the linearized system on each Newton iteration can be written in terms of the currently known displacement and Cauchy stress:

$$\begin{aligned}\mathbf{R}^{\mathbf{F}} = &\sum_{e\in\chi}\int_e \mathbf{L}^{\mathbf{T}}\sigma\,dv - \sum_{\gamma\in S_i}\int_\gamma [\mathbf{N}^{\mathbf{T}}]\mathbf{n}\{\sigma\}\,ds + \sum_{\gamma\in S_i}\frac{\delta_p G_0}{h_0}\int_\gamma [\mathbf{N}^{\mathbf{T}}]\\ &\times[u]\,ds - \sum_{e\in\chi}\int_E \mathbf{N}^{\mathbf{T}}\mathbf{b}\,dv - \sum_{\gamma\in\Gamma^t}\int_\gamma \mathbf{N}^{\mathbf{T}}\,\bar{t}\,ds\\ &+\sum_{\gamma\in\Gamma^p}\int_\gamma p\mathbf{N}^{\mathbf{T}}\vec{n}\,ds, \end{aligned} \tag{49}$$

where σ in (49) is now written as an algebraic vector, $\mathbf{n}$ is the matrix form of the normal vector, and $\vec{n}$ is the vector form of the normal vector.

On each Newton's iteration we solve the algebraic system of equations

$$\mathbf{K}\Delta\mathbf{U} = -\mathbf{R}^{\mathbf{F}}.$$

For DG implementation and programming, we follow the nodal-based DG implementation documented in detail in [28,31]. This nodal-based DG implementation is able to fully exploit existing popular CG finite element programs for finite deformation problems through simply breaking continuous elements and adding additional stiffness and internal force contributed from interior face and boundary face integrals. Three dimensional isoparametric elements are implemented in our IIPG computer code. For traditional spatial CG finite element framework and the updated Lagrange formulations for finite deformation problems, we refer to [5,8] for isoparametric element technology, stiffness and residual computation, implementation on pressure loading, and updating on geometry and state variables. In our spatial DG implementation, an initial meshing or initial nodal coordinate ($X = x_0$) is first obtained in the reference configuration. The deformed mesh is obtained at any Newton's iteration through simply updating current nodal coordinates as $x^{n+1} = x_0 + u^{n+1}$ where u^{n+1} is the total displacement vector of the node at time step $n+1$. A node id, once assigned at the initial configuration, will not change (like material point in the sense of Lagrange). Once the displacement is known, all measurements can be updated through the deformation gradient F. It should be noted that as DG is still Galerkin-based method, the space of test function is the same as the solution. In this paper, trilinear functions are implemented for displacement interpolations in the 8-node hexahedral elements. Finally, we discuss nonlinear iteration procedures for solving finite deformation problems with DG methods. Similar to CG methods for finite deformation problems, solution procedures for DG methods also involve the initialization of field variables for starting the Newton–Raphson iterations, updating stress, computing consistent tangent modulus in the local material level, assembling the stiffness matrix and the residual force vector, and updating the spatial configuration. To avoid non-convergent runs due to the use of linear iterative solvers and large and constant loading steps, a sparse direct solver and an automatic loading reduction and increase scheme are implemented in this work. For example, if the number of iterations within a load step exceeds 10, the incremental load will be reduced by 50% and the nonlinear iteration will restart for this load step. We describe the nonlinear solution procedure for DG methods in Table 1. Three key ingredients deserve to be highlighted: (a) Nonlinear procedures for both hypoelastoplasticity and hyperelastoplasticity are addressed; (b) Co-rotational implementation for hypoelastoplasticity and multiplicative decomposition and implementation for hyperelastoplasticity are treated separately; and (c) Compared with CG methods, additional stress returning and updating work on face Gaussian integration points required for DG methods are underlined.

8. Numerical examples

In this section, we first derive an analytical solution for a simple hyperelastic bar problem undergoing finite deformation with the gravity load. We then compare the IIPG solution with this exact solution for the bar problem to verify the IIPG formulation and implementation. we further select two more complex problems

Table 1
DG nonlinear procedures for finite deformation problems.

Step 1: Initialize variables:
- *Loop over all Gauss integration points on both elements and surfaces*
  - $u^{n+1} = u^n$;
  - $x^{n+1} = x^n$;
  - $\sigma^{n+1} = \sigma^n$;
- *if hypo*
  - $\varepsilon'^{p^{n+1}} = \varepsilon'^{p^n}$;
  - $q'^{n+1} = q'^n$.
- *if hyper*
  - $C^{p^{n+1}} = C^{p^n}$;
  - $\bar{q}^{n+1} = \bar{q}^n$.

Step 2: Predict incremental displacement:
- *Compute* : K *and* $R^F = -\Delta F^{ext}$
- ($K = K^e$ (*elastic*) *or* $K = K^n$);
- *solve* : $\Delta u = -K^{-1}R^F$;
- *update* : $x^{n+1} = x^n + \Delta u$;
- *update* : $u^{n+1} = u^n + \Delta u$;
- *obtain* : $F^{n+1} = I + \mathbf{Grad}(u^{n+1})$.

Step 3: Return stress
- *if hypo*:
  - *Compute* : R^{n+1} *according to* Eq. (43);
  - *Pull back* : $\Delta\varepsilon'$ *according to* Eq. (44);
  - *Return mapping* : $(\sigma'^{n+1}, \varepsilon_e'^{n+1}, \varepsilon_p'^{n+1}, q'^{n+1}, \mathbf{c}'^{n+1})$;
  - (*according to material integrator I documented in* [32]);
  - *Push forward* : $(\sigma'^{n+1}, \mathbf{c}'^{n+1}) \rightarrow (\sigma^{n+1}, \mathbf{c}^{n+1})$ *according to* Eq. (45).
- *if hyper*:
  - *Return Mapping* : $(\sigma^{n+1}, C^{p^{n+1}}, \mathbf{c}^{n+1})$
  - (*according to material integrator II documented in* [8];
  - (*Page* : 212 − −214)).

Step 4: Update Δu:
- *compute* : K *and* R^F *according to Eq.*(48) *and Eq.*(49);
- *correct* : $\Delta u = \Delta u - K^{-1}R^F$;
- *update* : $x^{n+1} = x^n + \Delta u$;
- *update* : $u^{n+1} = u^n + \Delta u$;
- *obtain* : $F^{n+1} = I + \mathbf{Grad}(u^{n+1})$.

Step 5: Check residual:
- *if* $L^2(R^F) \geqslant TOL$, *go to* **Step 3**.
- *if* $n+1 = n^{max}$, **Exit** *or go to* **Step 1** *for next load step.*

suitable to evaluate the performance of our IIPG method for solving both hypoelastoplastic and hyperelastoplastic problems. For testing hypoelastoplastic problems, in addition to the plasticity factor, the effect of large rotation on convergence rates should also be evaluated. A cantilever beam problem designed to have less stress-concentration on its boundaries and being able to undergo large rotation is selected to serve such a purpose. This beam is also resolved by using a hyperelastoplastic model and by applying pressure loading. The DG performance is further evaluated using a bipolar void growth and coalescence problem, which was first solved in [35] for evaluating the formulation of the implicit finite element methods for multiplicative plasticity in the framework of CG methods. It should me mentioned that as only isoparametric hexahedral elements are implemented in our computer code, all plain strain problems presented in this paper are solved through restraining the degree of freedom in a specified direction.

8.1. A hyperelastic bar with gravity load

In this section, we verify the IIPG formulation and implementation through developing an analytical solution for a hyperelastic bar problem subjected to a gravity load. The convergence rate of the IIPG method towards the exact solution in terms of the total number of meshed elements is studied. The convergence for Newton's iterations is also presented.

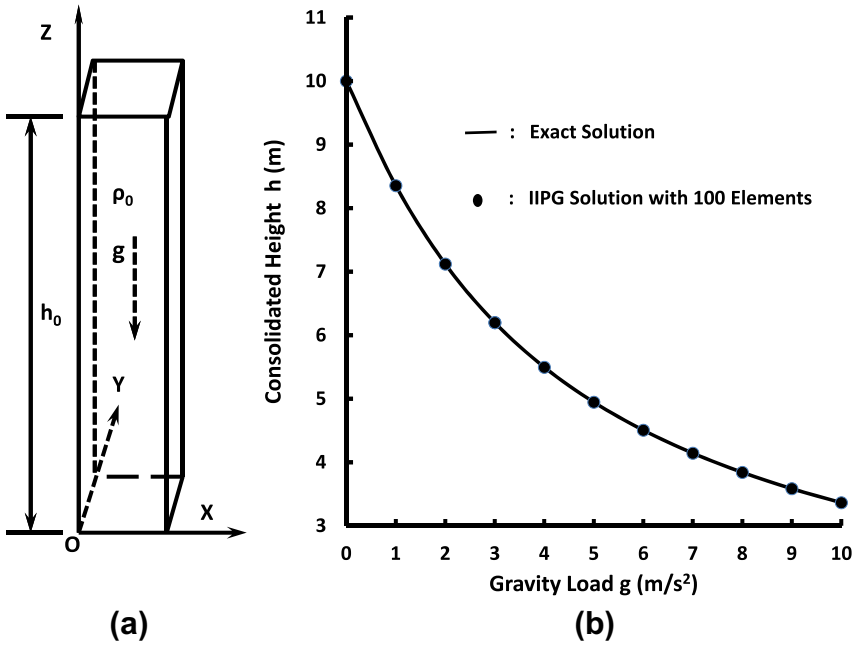

Fig. 3. A hyperelastic bar under gravity load: (a) bar geometry and (b) exact and IIPG consolidated heights versus gravity load.

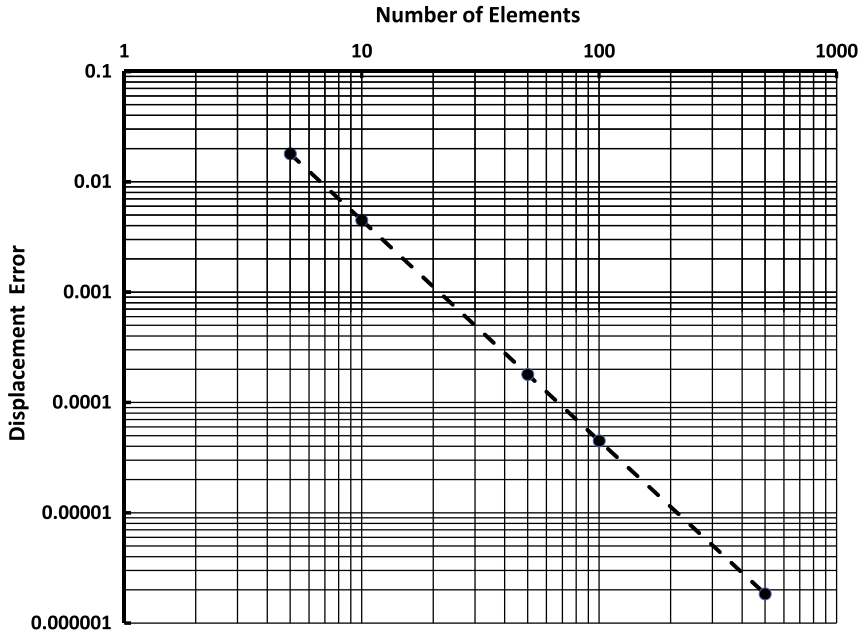

Fig. 4. Displacement error of the IIPG method versus element numbers for hyperelastic bar problem: error defined by $|h^{IIPG} - h_0|/h_0$; load level at $g = 10\ \mathrm{m/s^2}$; and log (base 10) scale for both axes.

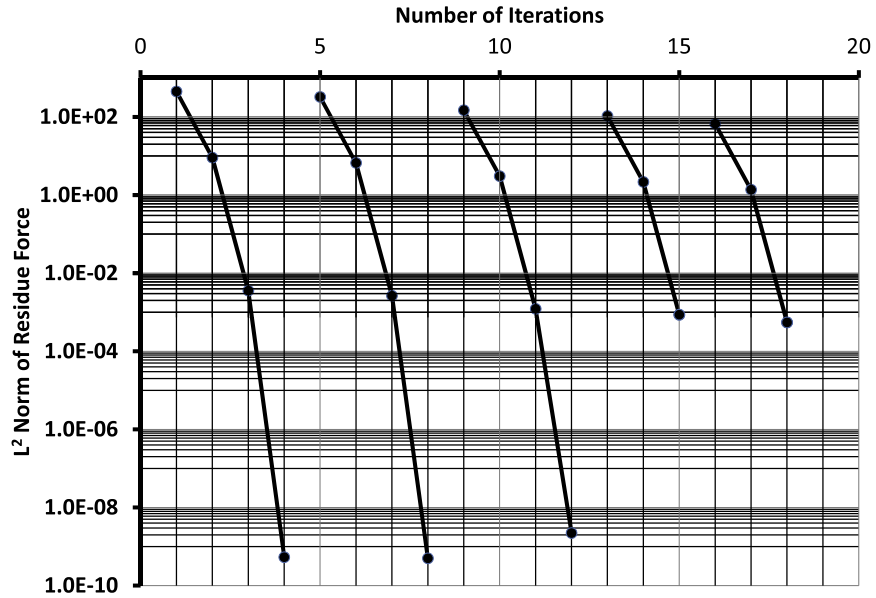

Fig. 5. Norms of force residual versus iteration number: curves from the left to the right are corresponding to 5, 10, 50, 100, and 500 elements at last load step ($g = 10\ \mathrm{m/s^2}$); curves are technically shifted; convergence tolerance is 1.0e−3.

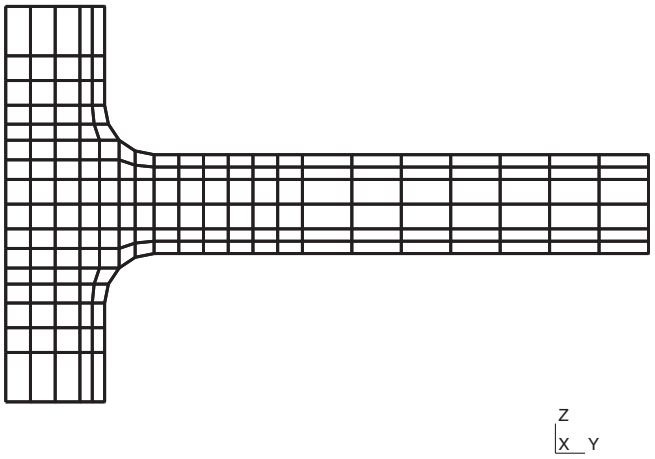

Fig. 6. Profile and finite element mesh of cantilever beam problem.

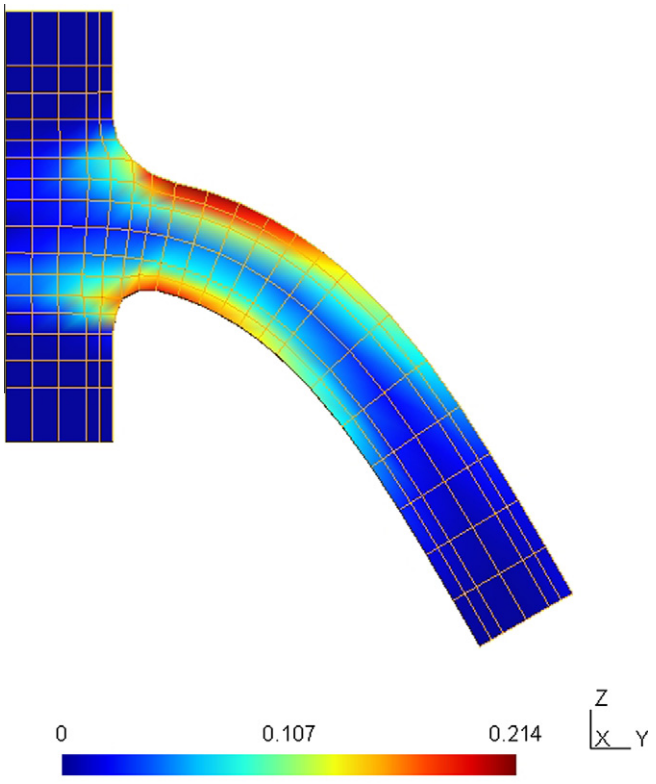

Fig. 7. Contour of equivalent plastic strain for cantilever beam problem with hypoelastoplastic materials at full loading level.

A quarter model of the bar with square cross-section is plotted in Fig. 3. In Fig. 3, the initial height and material initial density for the bar, defined at the condition of the gravity $g = 0$, are denoted by h_0 and ρ_0. The material is assumed to follow the neo-Hookean law: $\sigma = \mu(b - I)/J + \lambda \ln^J/J$ where μ and λ are material shear modulus and Lame constant. We further assume that $\lambda = 0$, which substantially simplifies this problem into a one dimensional problem. More precisely, only vertical displacement component in displacement field is non-zero. Hence, the vertical component of the deformation gradient F, the left Cauchy–Green strain tensor, and the Jacobian of the deformation gradient F can be simply written in terms of the vertical displacement $u(Z)$ as follows:

$$F_Z = 1 + \frac{du(Z)}{dZ}; \quad b_z = \left(1 + \frac{du(Z)}{dZ}\right)^2; \quad J = 1 + \frac{du(Z)}{dZ}.$$

The unknown $u(Z)$ is obtained through solving a second-order ordinary differential equation formulated in the reference configuration B_0 as follows:

$$\begin{cases} \frac{dP_Z}{dZ} + \rho_0 g = 0 \quad (\textit{Equilibrium Equation}); \\ P_Z = J\sigma_z/F_Z \quad (\textit{Stress Pull} - \textit{Back}); \\ \sigma_z = \mu(b_z - 1)/J \quad (\textit{Material Law}), \end{cases} \tag{50}$$

with boundary conditions:

$$\begin{cases} u(Z)|_{Z=0} = 0; \\ \frac{du(Z)}{dZ}|_{Z=h_0} = 0, \end{cases} \tag{51}$$

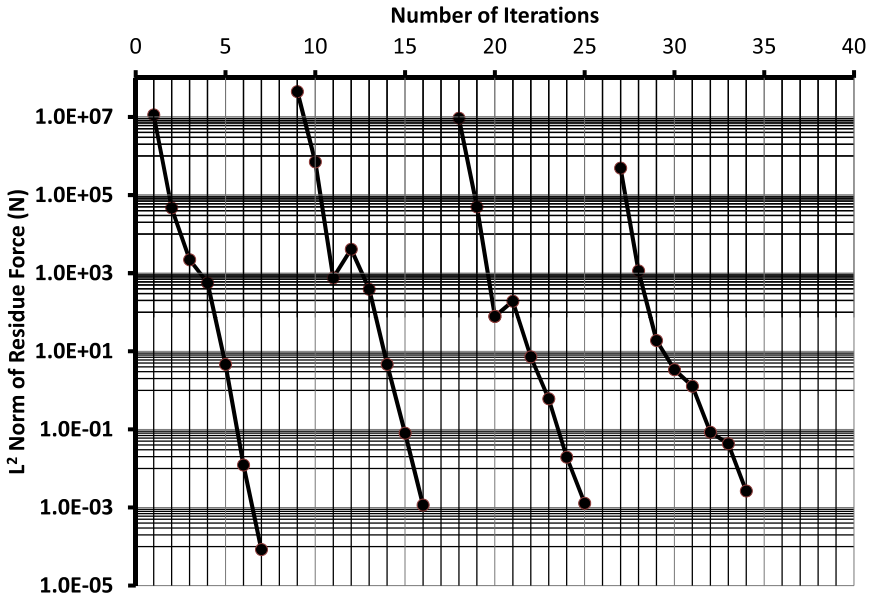

Fig. 8. Norms of residual forces in global Newton–Raphson iterations for cantilever problem with hypoelastoplastic model: curves from the left to the right are corresponding to load levels at percent, 10%, 50%, and 100%; curves are technically shifted; convergence tolerance is 1.0e−2.

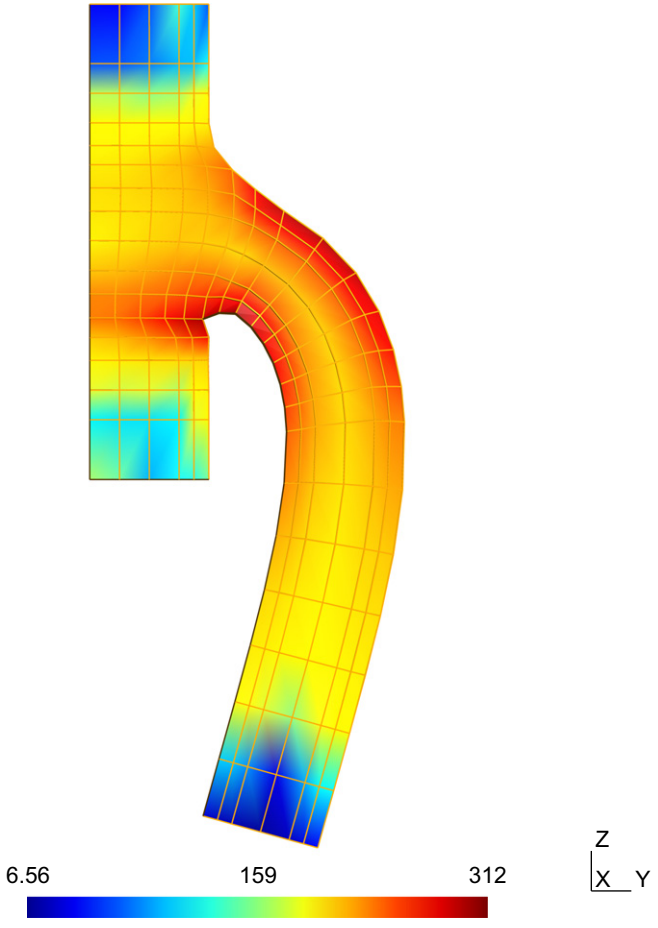

Fig. 9. Contour of von Mises stress for cantilever beam problem with hyperelastoplastic materials and under pressure loading at full loading level.

where P_Z and σ_z are the normal components in the vertical direction of the first Piola–Kirchhoff stress and the Cauchy stress tensors, respectively.

Finally, the displacement solution $u(Z)$ for this bar problem is given by:

$$u(Z) = \frac{Z-h_0}{4}\sqrt{\beta^2(Z-h_0)^2+4} + \frac{1}{\beta}ln^{\left\{\beta(Z-h_0)+\sqrt{\beta^2(Z-h_0)^2+4}\right\}} + \frac{h_0}{4}\sqrt{\beta^2h_0^2+4} - \frac{1}{\beta}ln^{\left\{\sqrt{\beta^2h_0^2+4}-\beta h_0\right\}} + \frac{\beta(Z-h_0)^2}{4} - \frac{\beta h_0^2}{4} - Z, \tag{52}$$

where $\beta = \rho_0 g/\mu$ and has a unit of the inverse of length. Inserting $Z = h_0$ into (52), we obtain $h = h_0 + u(Z = h_0)$, the consolidated height of the bar, as follows:

$$h = \frac{1}{\beta}ln^{\left\{\frac{2}{\sqrt{\beta^2(Z-h_0)^2+4}-\beta h_0}\right\}} + \frac{h_0}{4}\sqrt{\beta^2h_0^2+4} + \frac{\beta h_0^2}{4}. \tag{53}$$

The quarter model of the bar shown in Fig. 3(a) is constrained at $X = 0$ for X-direction displacement, at $Y = 0$ for Y-direction displacement, and at $Z = 0$ for Z-direction displacement. The initial height, initial density, material shear modulus, and maximum gravity load are given by $h_0 = 10\ m$, $\rho = 1500\ \mathrm{kg/m^3}$, $\mu = 20000\ \mathrm{N/m^2}$, and $g = 10\ \mathrm{m/s^2}$. The bar is uniformly meshed into 5, 10, 50, 100, and 500 discontinuous segments along the vertical direction. The gravity load is equally divided by 50 load steps. In Fig. 3(b), the consolidated height versus the increase in gravity load predicted from the IIPG method with 100 elements is compared with the exact solution. In detail, IIPG predicts $h = 3.364700$ m and the exact solution gives $h = 3.364851$ m at gravity load $g = 10\ \mathrm{m/s^2}$. This shows that the IIPG method predicts very accurate results. To further study the convergence rate towards the exact solution for the IIPG method, we run other four different meshes mentioned above. Fig. 4 presents the error of relative consolidated height in terms of the number of elements. The error is defined by $|h^{IIPG} - h_0|/h_0$ and the logarithmic scale with base 10 for both axes is used. We observe a strict linear convergence rate for the IIPG method for solving this hyperelastic bar problem with gravity load. To study convergence patterns for Newton's iterations, we present the norms of residual force in Fig. 5. In Fig. 5, the five curves are corresponding to five different meshes at the last load step (towards $g = 10\ \mathrm{m/s^2}$). It should be noted that last four curves in Fig. 5 are technically shifted so that

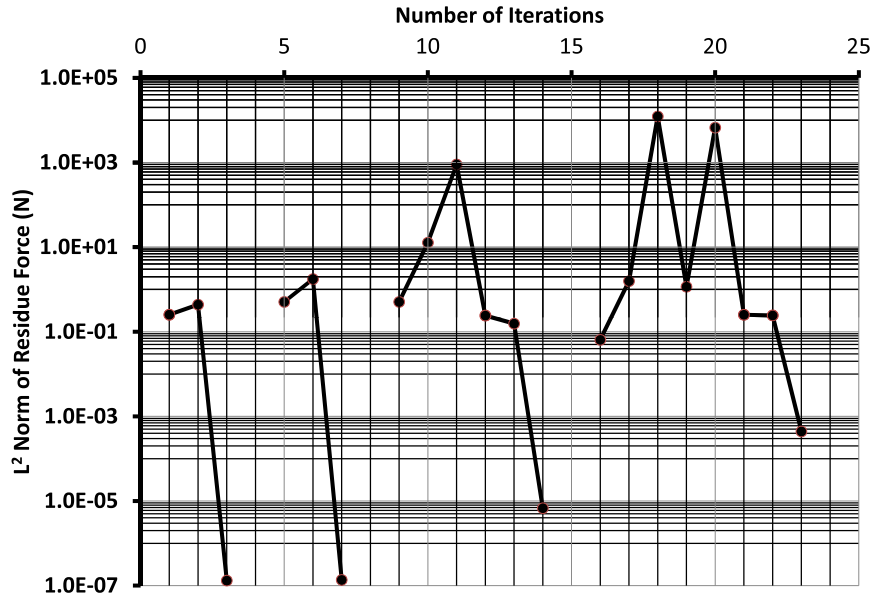

Fig. 10. Norms of residual forces in global Newton–Raphson iterations for cantilever problem with hyperelastoplastic model: curves from the left to the right are corresponding to load levels at 1%, 10%, 50%, and 100%; curves are technically shifted; convergent tolerance is 1.0e−3.

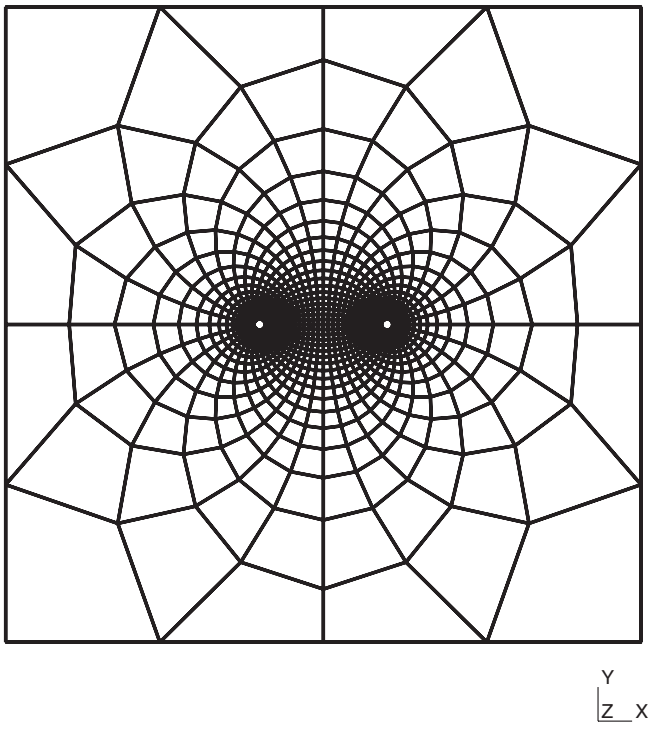

Fig. 11. Profile and initial mesh configuration of bipolar void growth and coalescence problem.

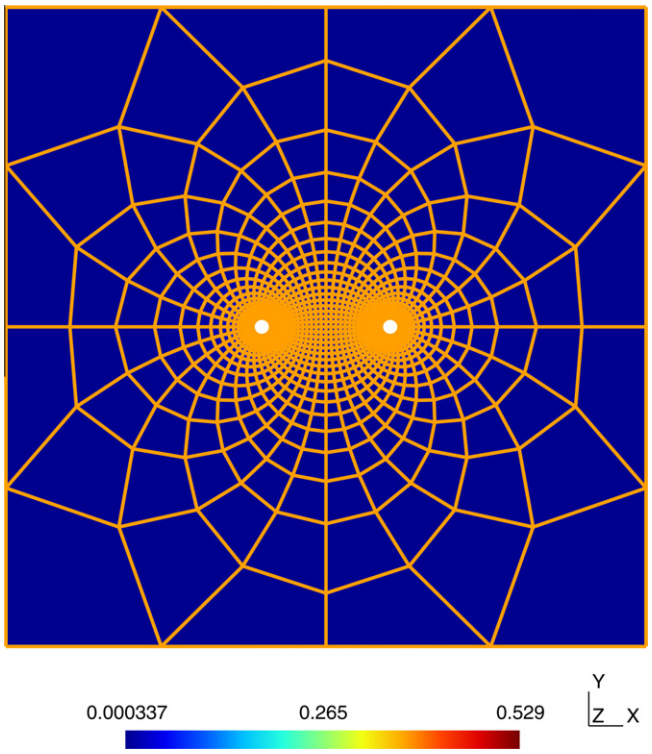

Fig. 12. Deformation and equivalent plastic strain contour for bipolar void growth and coalescence problem (Loading Level: 2.5 Percent).

the five curves for different meshes can be compactly plotted in one graph. Strict quadratic convergence rates for Newton's iterations are observed in these IIPG runs for this relatively simple bar problem. In the next subsections, two more problems with more complex geometries, material models, and load conditions are selected to further evaluate the performance of the IIPG method.

8.2. A cantilever beam under finite deformation

A cantilever beam with a length of 55 mm and a height of 10 mm is shown in Fig. 6. It is constrained in the horizontal direction (y-axis) at its left end, in the vertical direction at the top and bottom surfaces of the left end, and in the x-direction on the surface at $x = 0$. The beam is meshed into 170 hexahedral elements and 1360 nodes. We first solve this beam problem with hypoelastoplastic materials to evaluate the performance of the IIPG method. In this run, we apply a displacement controlled load up to $\delta u = 40$ mm at the nodes on the tip top line, which implies that the beam will undergo both large strain and large rotation. The material elastic constants are: $E = 210$ Mpa (the Young Modulus) and

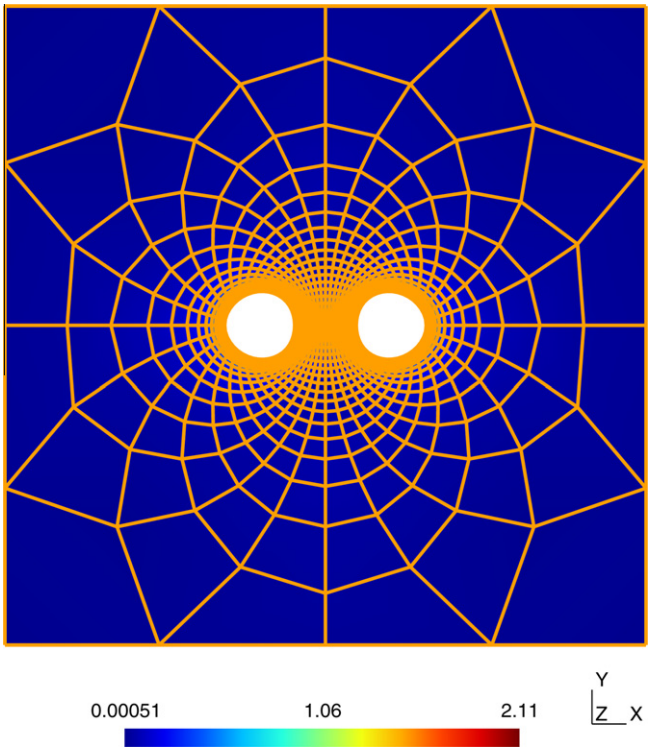

Fig. 13. Deformation and equivalent plastic strain contour for bipolar void growth and coalescence problem (Loading level: 10%).

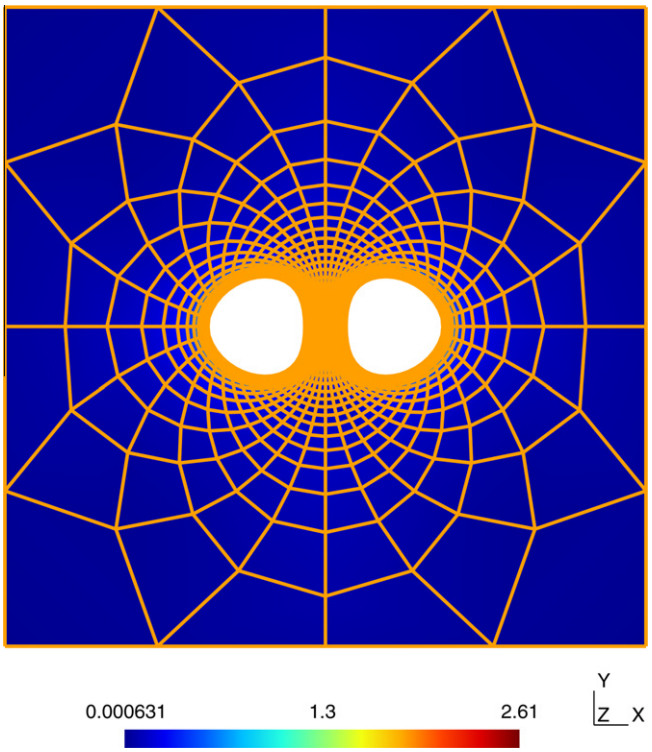

Fig. 14. Deformation and equivalent plastic strain contour for bipolar void growth and coalescence problem (Loading level: 20%).

$\mu = 0.499$ (the Poison ratio). Classic J_2 plasticity with bilinear hardening behavior is assumed for the beam material.

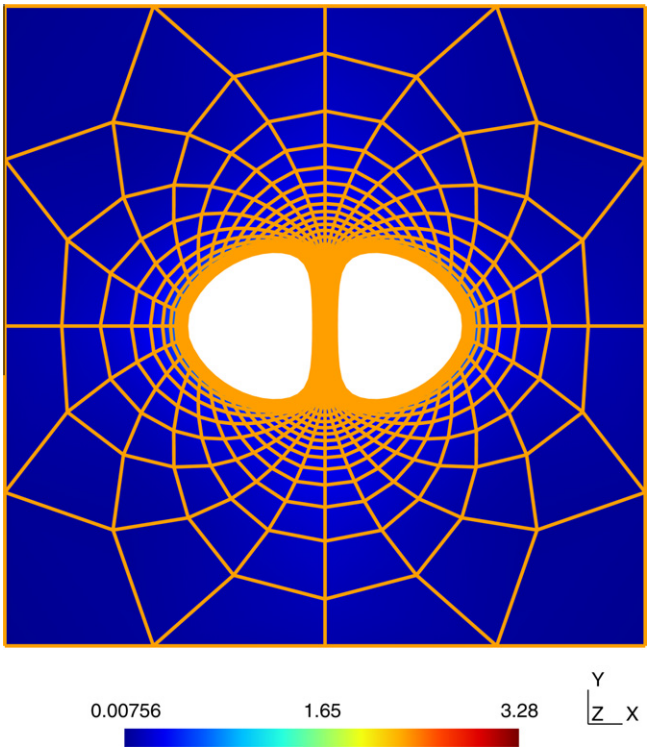

Fig. 15. Deformation and equivalent plastic strain contour for bipolar void growth and coalescence problem (Loading level: 40%).

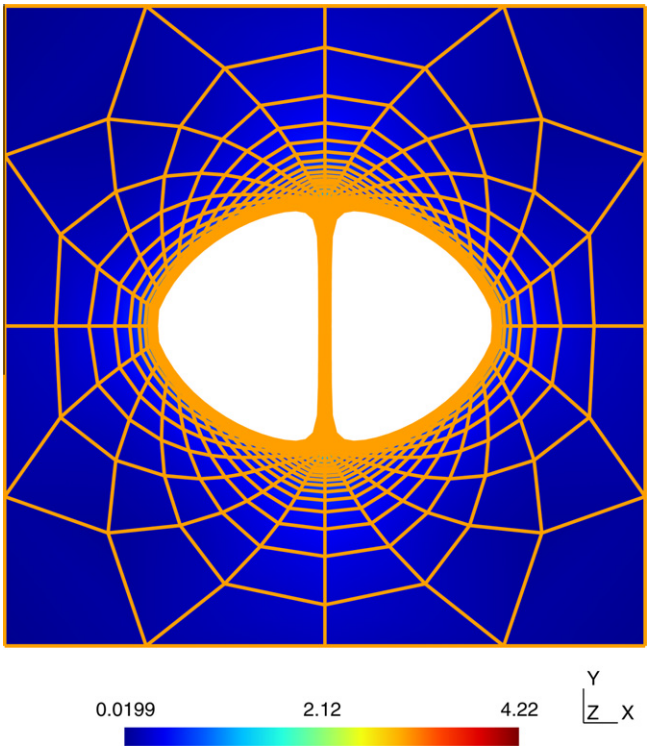

Fig. 16. Deformation and equivalent plastic strain contour for bipolar void growth and coalescence problem (Loading level: 80%).

The yield stress is $\sigma_0 = 200$ Mpa. The hardening modulus is $H = 210$ Mpa. The loading is initially divided into 200 load steps but the actual load steps is up to 382 for a complete run. Fig. 7

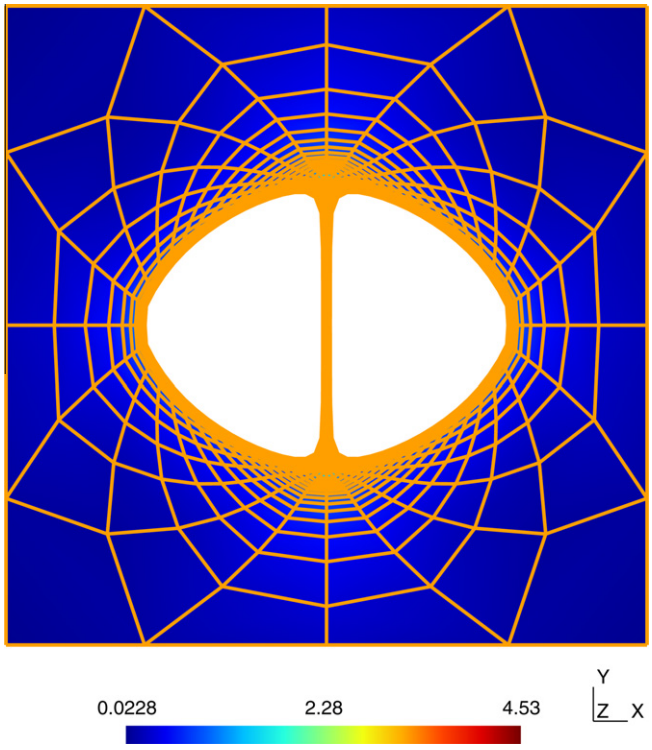

Fig. 17. Deformation and equivalent plastic strain contour for bipolar void growth and coalescence problem (Loading level: 100%).

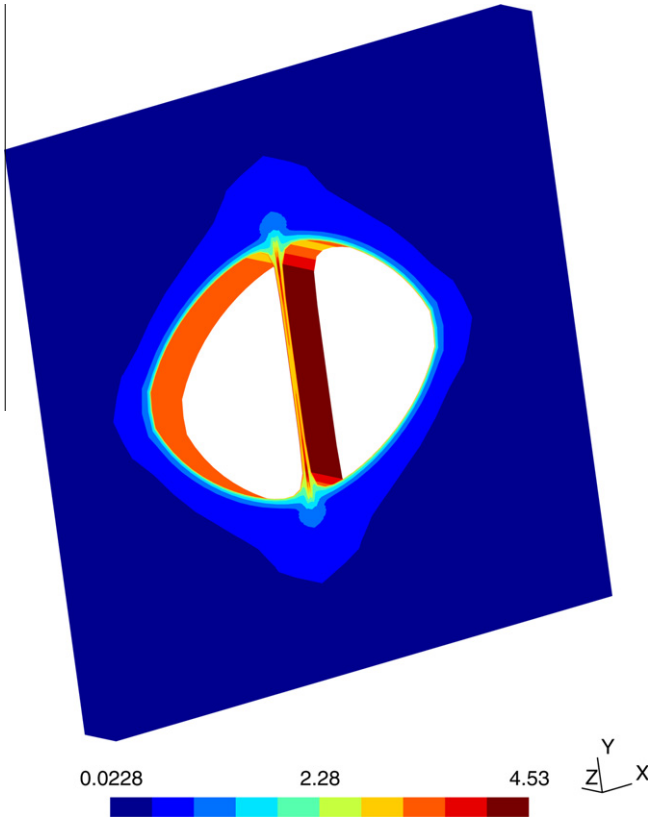

Fig. 18. Deformation and equivalent plastic strain contour for bipolar void growth and coalescence problem (Loading level: 100%; Ligament stretching profile).

shows the deformation configuration of the beam. The equivalent plastic strain with maximum value up to 0.21 is also contoured in Fig. 7. The L^2 norms of the force residual vector at the selected four load levels are presented in Fig. 8. We conclude that a quadratic convergence rate for Newton's iterations is observed at low load levels but the convergence deteriorates at the stages where large deformation or rotation substantially develops. However, the deteriorated convergence rates are still fast as each load step is finished within 8 iterations. To our knowledge this convergence pattern for DG methods in the co-rotational framework for hypoelastoplasticity undergoing large deformation is similar to the tradition CG methods where strict quadratic convergence rates are often lost when deformation is large.

This beam problem is resolved to test the DG performance in the framework of multiplicative formulation for materials with hyperelastoplastic models. The material constants for the nearly incompressible neo-Hookean material model are: $\lambda = 0.7e + 7$ Mpa and $\mu = 0.7e + 5$ Mpa. The plasticity parameters are assumed to be the same as the previous hypoelastoplastic case. Moreover, in this study we apply pressure loading $p = 12.5$ Mpa on the top surface of the beam so that the DG formulation taking into account the pressure effect will be also tested in the multiplicative framework. It should be noted that in this pressure load case the beam local stress paths are highly non-proportional due to the follower load and the large rotation of the structure. The loading is initially divided by 200 steps and the actual number of loading steps is 229. The deformation and the Von Mises stress of the beam with hyperelastoplastic materials are presented and contoured in Fig. 9. Fig. 10 shows the L^2 norms of the residual force for the selected load levels. From this Figure we see that strict quadratic convergence rates are observed for all load steps.

8.3. A bipolar void growth and coalescence problem

In this section, we apply the IIPG method to solve void growth and coalescence problems, which are important in material damage and failure research and applications. On microscopic scale levels, the damage and ductile fracture of metal materials result from the nucleation, growth, and coalescence of voids embedded in metal solid matrices [16,37,15]. Even though structures undergo only a small deformation from the point of macroscopic view, the local strain developed near voids may be several thousand times over the global strain. This brings a challenge for the study of the void growth through employing necessary computational approaches as the phenomenon of the void growth is an inherently finite deformation problem in microscopic scales. As a pioneering example, the detailed growth and coalescence profile for two bipolar voids was first investigated by Moran, Ortiz, and Shih in [35] through applying their proposed CG-based multiplicative formulation to finite hyperelastoplastic problems. We use this problem to further demonstrate the performance of our proposed IIPG method for solving hyperelastoplastic problems.

As shown in Fig. 11, the structure has two voids modeled by two identical hollow cylinders with circular sections embedded in a metal solid matrix. The plane strain condition is assumed in our analysis. The initial distance between the two centers of the voids is 2 mm, the diameter of the void 0.1733 mm, and the length of the squared cross-section of the solid matrix 5 mm. The neo-Hookean hyperelastic material constants are: $\lambda = 9.396e + 4$ Mpa and $\mu = 7.047e + 4$ Mpa. The J_2 plasticity parameters are $\sigma_0 = 35.235$ Mpa and $H = 0.35235$, which indicates that a nearly ideal plasticity is assumed for solid matrix materials in this study. We apply a displacement-controlled loading $\delta_u = 0.5$ mm on the remote surfaces. To avoid any potential needs on re-meshing due to serious distortions of the original mesh in the case of very large strain developed at higher loading levels, we follow the idea described in [35] and design an initially orthogonal mesh using bipolar coordinates. Eventually, a total of 397 8-node hexahedral elements and 3176 nodes are produced in the quarter model

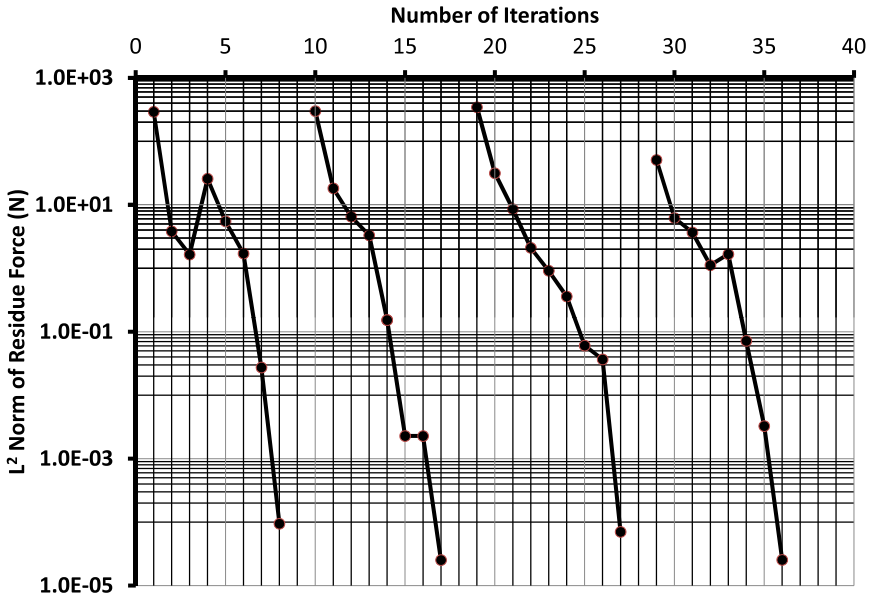

Fig. 19. Norms of residual forces in Global Newton–Raphson iterations for bipolar void coalescence problem with hyperelastoplastic model: curves from the left to the right are corresponding to load levels at 1%, 10%, 50%, and 100%; curves are technically shifted; convergence tolerance is 1.0e−3.

shown in Fig. 11. As the plane strain is assumed in the analysis, all the degrees of freedom in the z-direction are constrained. A total of 400 initial loading steps are predefined in the run but the final loading stage of the deformation is successfully finished in 440 load steps through employing an automatic loading step adjustment strategy.

Figs. 12–17 present the details of the void growth corresponding to six different loading levels. The initial volume of each void is 0.024136 mm^3 and the final volume of the void is 10.4 mm^3, which indicates that the void grows 431 times. On the other hand, the wall thickness between the two voids shrinks from 1.8343 mm to 0.1295 mm, 93% in thickness reduction. Because of the whole cross-section of the structure and the solid matrix material with nearly ideal plasticity, the 0.1295 mm residual thickness of the ligament between the two voids may have little contribution to the capacity change of the whole structure. From this point of view, this ligament could be removed and the two voids would coalesce into a larger single void. Another strong evidence for the removal of this narrowed ligament is the equivalent plastic strain contour shown in Fig. 18. From Fig. 18, we see that the maximum equivalent plastic strain develops in the narrowed ligament and reaches a value of 453%. The distribution of the plastic strain is uniform over almost the whole ligament between the two voids. Moreover, a new larger coalesced void with an elliptic cross-section may be expected from the removal of the narrowed ligament between the two growing voids. Finally, Fig. 19 presents the profile of the convergence for Newton's iterations for the void growth problem solved by the IIPG method. We conclude that quadratic convergence rates are achieved for our IIPG implementation for this bipolar void problem undergoing very large deformation.

9. Conclusions

A spatial formulation of the IIPG method has been established for solving both hypoelastoplastic and hyperelastoplastic problems with finite deformation. The formulation of the IIPG method has been derived in the co-rotational framework and in the intermediate configuration through consistently linearizing DG weak formulation for general nonlinear solid mechanics problems including the pressure loading case. Two new terms, the surface geometric stiffness and surface penalty geometric stiffness, have been introduced in this DG spatial formulation. The performance of the IIPG method is demonstrated through solving a beam problem and a bipolar void growth problem with finite elastoplastic deformation. Fast convergence rates for Newton's iteration are observed in our IIPG formulation.

References

[1] N. Aravas, On the numerical integration of a class of pressure-dependent plasticity models, Int. J. Numer. Methods Engrg. 24 (1987) 1395–1416.
[2] D.N. Arnold, An interior penalty finite element method with discontinuous Elements, SIAM J. Numer. Anal. 19 (1982) 742–760.
[3] D.N. Arnold, F. Brezzi, B. Cockburn, L.D. Marini, Unified analysis of discontinuous Galerkin methods for elliptic problems, SIAM J. Numer. Anal. 39 (2002) 1749–1779.
[4] G.A. Baker, Finite element methods for elliptic equations using nonconforming elements, Math. Comput. 31 (1977) 45–59.
[5] K.J. Bathe, Finite Element Procedures, Printice Hall, New Jersey, 1996.
[6] T. Belytschko, W.K. Liu, B. Moran, Nonlinear Finite Elements for Continua and Structures, John Wiley, 2000.
[7] C.E. Baumann, J.T. Oden, A discontinuous hp finite element method for the Euler and Navier-Stokes equations, Int. J. Numer. Methods Fluids 31 (1999) 79–95.
[8] J. Bonet, R.D. Wood, Nonlinear Finite Elements for Continua and Structures, John Wiley, 2000.
[9] B. Cockburn, C. Shu, The local discontinuous Galerkin finite element method for convection-diffusion systems, SIAM J. Numer. Anal. 35 (1998) 2440–2463.
[10] B. Cockburn, G.E. Karniadakis, C. Shu, Discontinuous Galerkin Methods: Theory, Computation and Application, Springer, Verlag, 2000.
[11] C.N. Dawson, S. Sun, M.F. Wheeler, Compatible Algorithms for coupled flow and transport, Comput. Methods Appl. Mech. Engrg. 193 (2004) 2565–2580.
[12] J.K. Djoko, F. Ebobisse, A.T. McBride, B.D. Reddy, A discontinuous Galerkin formulation for classical and gradient plasticity. Part 1: Formulation and analysis, Comput. Methods Appl. Mech. Engrg. 196 (2007) 3881–3897.
[13] J.K. Djoko, F. Ebobisse, A.T. McBride, B.D. Reddy, A discontinuous Galerkin formulation for classical and gradient plasticity. Part 2: Algorithms and numerical analysis, Comput. Methods Appl. Mech. Engrg. 197 (2007) 1–21.
[14] J. Douglas, T. Dupont, Interior penalty procedures for elliptic and parabolic Galerkin methods, Lect. Notes Phys. 58 (1976) 207–216.
[15] X. Gao, J. Kim, Modeling of ductile fracture: significance of void coalescence, Int. J. Solids Struct. 43 (2006) 6277–6293.
[16] A.L. Gurson, Continuum theory of ductile rupture by void nucleation and growth: Part I-Yield criterion and flow rules for porous ductile media, J. Engrg. Mater. Technol. 1 (1977) 2–15.
[17] M.E. Gurtin, An Introduction to Continuum Mechanics, Academic Press, New Yok, 1981.

[18] P. Hansbo, M.G. Larson, Discontinuous Galerkin method for incompressible and nearly incompressible elasticity by Nitsche's methods, Comput. Methods Appl. Mech. Engrg. 191 (2002) 1895–1908.
[19] P. Hansbo, A discontinuous finite element method for elasto-plasticity, Int. J. Numer. Methods Biomedical Engrg. 26 (2008) 780–789.
[20] H.D. Hibbitt, Some follower force and load stiffness, Int. J. Numer. Methods Engrg. 14 (1979) 937–941.
[21] A. Hoger, D.E. Carlson, Determination of the stretch and rotation in the polar decomposition of the deformation gradient, Quart. Appl. Math. 42 (1984) 113–117.
[22] A. Hoger, D.E. Carlson, On the derivative of the square root of a tensor and Guo's rate theorems, J. Elasticity 14 (1984) 329–336.
[23] G.A. Holzapfel, Nonlinear Solid Mechanics, Wiley, New York, 2004.
[24] T.J.R. Hughes, K.S. Pister, Consistent linearization in mechanics of solids and structures, Comput. Struct. 9 (1978) 391–397.
[25] R.D. Krieg, D.B. Krieg, Accuracies of numerical solutions methods for elastic-perfectly plastic model, J. Pressure Vessel Technol. 99 (1977) 510–515.
[26] A. Lew, P. Neff, D. Sulsky, M. Ortiz, Optimal BV estimates for a discontinuous Galerkin method for linear elasticity, Appl. Math. Res. Express 3 (2004) 73–106.
[27] R. Liu, Discontinuous Galerkin finite element solution for poromechanics problem, Ph.D. dissertation, The University of Texas at Austin, 2004.
[28] R. Liu, M.F. Wheeler, C. Dawson, A three-dimensional nodal-based implementation of a family of discontinuous Galerkin methods for elasticity, Comput. Struct. 87 (2009) 141–150.
[29] R. Liu, M.F. Wheeler, C. Dawson, R. Dean, Modeling of convection-dominated thermoporomechanics problems using incomplete interior penalty Galerkin method, Comput. Methods Appl. Mech. Engrg. 198 (2009) 912–919.
[30] R. Liu, M.F. Wheeler, C. Dawson, R. Dean, On a coupled discontinuous/continuous Galerkin framework and an adaptive penalty scheme for poroelasticity problems, Comput. Methods Appl. Mech. Engrg. 198 (2009) 3499–3510.
[31] R. Liu, M.F. Wheeler, C.N. Dawson, R. Dean, A fast convergent rate preserving discontinuous Galerkin framework for rate-independent plasticity problems, Comput. Methods Appl. Mech. Engrg. 199 (2010) 3213–3226.
[32] J.E. Marsden, T.J.R. Hughes, Mathematical Foundations of Elasticity, Prentice Hall, Englewood Cliffs, N.J., 1984.
[33] A.T. McBride, B.D. Reddy, A discontinuous Galerkin formulation of a model of gradient plasticity at finite strains, Comput. Methods Appl. Mech. Engrg. 198 (2009) 1805–1820.
[34] L. Molari, G.N. Wells, K. Garikipati, F. Ubertini, A discontinuous Galerkin method for strain gradient-dependent damage: study of interpolations and convergence, Comput. Methods Appl. Mech. Engrg. 195 (2006) 1480–1498.
[35] B. Moran, M. Ortize, C.F. Shih, Formulations of implicit finite element methods for multiplicative finite deformation plasticity, Int. J. Numer. Methods Engrg. 29 (1990) 483–514.
[36] J.C. Nagtegaal, On the implementation of inelastic constitutive equations with special reference to large deformation problems, Comput. Methods Appl. Mech. Engrg. 93 (1982) 253–273.
[37] A. Needleman, V. Tvergaard, An analysis of ductile rupture in notched bars, J. Mech. Phys. Solids 32 (1984) 461–490.
[38] J. Nitsche, Über ein Variationsprinzip zur Lösung von Dirichlet bei Verwendung von Teilräumen, die keinen Randbedingungen unterworfen sind, Abh. Math. Univ. Hamburg 36 (1970) 9–15.
[39] L. Noels, R. Radovitzky, A general discontinuous Galerkin method for finite hyperelasticity. Formulation and numerical applications, J. Numer. Methods Engrg. 68 (2006) 64–97.
[40] J.T. Oden, Finite Elements of Nonlinear Continua, McGraw-Hill, New Your, 1972.
[41] J.T. Oden, I. Bubuska, C.E. Baumann, A discontinuous hp finite element method for diffusion problems, J. Comput. Phys. 146 (1998) 491–519.
[42] R.W. Ogden, Non-linear Elastic Deformations, Ellis Horwood, Chichester, 1984.
[43] M. Ortiz, E.P. Popov, Accuracy and stability of integration algorithms for elastoplastic constitutive relations, Int. J. Numer. Methods Engrg. 21 (1985) 1561–1576.
[44] B. Riviere, S. Shaw, M.F. Wheeler, J.R. Whiteman, Discontinuous Galerkin finite element methods for linear elasticity and quasistatic linear viscoelasticity, Numer. Math. 95 (2003) 347–376.
[45] Y. Shen, A. Lew, An optimally convergent discontinuous-Galerkin-based extended finite element method for fracture mechanics, Int. J. Numer. Methods Engrg. 82 (2010) 716–755.
[46] J.C. Simo, R.L. Taylor, Consistent tangent operators for rate-independent elastoplasticity, Comput. Methods Appl. Mech. Engrg. 48 (1985) 101–118.
[47] J.C. Simo, T.J.R. Hughes, General returning mapping algorithms for rate independent plasticity, in: C.S. Desai (Ed.), Constitutive Equations for Engineering Materials, 1987.
[48] J.C. Simo, S. Govindjee, Non-linear B-stability and symmetry preserving return mapping algorithms for plasticity and viscoplasticity, Int. J. Numer. Methods Engrg. 31 (1991) 151–176.
[49] J.C. Simo, T.J.R. Hughes, Computational Inelasticity, Springer-Verlag, New York, 1998.
[50] A. Ten Eyck, A. Lew, Discontinuous Galerkin methods for nonlinear elasticity, J. Numer. Methods Engrg. 67 (2006) 1204–1243.
[51] A. Ten Eyck, F. Celiker, A. Lew, Adaptive stabilization of discontinuous Galerkin methods for nonlinear elasticity, analytical estimates, Comput. Methods Appl. Mech. Engrg. 197 (2008) 2989–3000.
[52] T.T. Ting, Determination of C1/2, C-1/2 and more general isotropic tensor functions of C, J. Elasticity 15 (1985) 319–323.
[53] C. Truesdell, W. Noll, S. Antman, The Non-Linear Field Theories of Mechanics, third ed., Springer, 2004.
[54] G.N. Wells, K. Garikipati, L. Molari, A discontinuous Galerkin formulation for a strain gradient-dependent continuum model, Comput. Methods Appl. Mech. Engrg. 193 (2004) 3633–3645.
[55] M.F. Wheeler, An elliptic collocation finite element method with interior penalties, SIAM J. Numer. Anal. 15 (1978) 152–161.
[56] T.P. Wihler, Locking-Free DGFEM for elasticity problems in polygons, IMA J. Numer. Anal. 24 (2004) 45–75.